

## **Final Report**

**Title: Diode laser sensor for scramjet inlets**

**AFOSR/AOARD Reference Number: AOARD- 08-4019**

**AFOSR/AOARD Program Manager: Dr Rengasamy Ponnappan**

**Period of Performance: 03/2008 – 03/2010**

**Submission Date: 11/05/2010**

**Principal Investigator:**

Dr Sean O'Byrne, University of New South Wales, Australian Defence Force Academy

Report Documentation Page			Form Approved OMB No. 0704-0188		
Public reporting burden for the collection of information is estimated to average 1 hour per response, including the time for reviewing instructions, searching existing data sources, gathering and maintaining the data needed, and completing and reviewing the collection of information. Send comments regarding this burden estimate or any other aspect of this collection of information, including suggestions for reducing this burden, to Washington Headquarters Services, Directorate for Information Operations and Reports, 1215 Jefferson Davis Highway, Suite 1204, Arlington VA 22202-4302. Respondents should be aware that notwithstanding any other provision of law, no person shall be subject to a penalty for failing to comply with a collection of information if it does not display a currently valid OMB control number.					
1. REPORT DATE <b>12 MAY 2010</b>		2. REPORT TYPE <b>Final</b>		3. DATES COVERED <b>01-03-2008 to 28-02-2010</b>	
4. TITLE AND SUBTITLE <b>Diode Laser Scramjet Inlet Sensor</b>				5a. CONTRACT NUMBER <b>FA48690814019</b>	
				5b. GRANT NUMBER	
				5c. PROGRAM ELEMENT NUMBER	
6. AUTHOR(S) <b>Sean O'Byrne</b>				5d. PROJECT NUMBER	
				5e. TASK NUMBER	
				5f. WORK UNIT NUMBER	
7. PERFORMING ORGANIZATION NAME(S) AND ADDRESS(ES) <b>University of New South Wales,Northcott Drive,Campbell,Australia,AU,ACT 2600</b>				8. PERFORMING ORGANIZATION REPORT NUMBER <b>N/A</b>	
9. SPONSORING/MONITORING AGENCY NAME(S) AND ADDRESS(ES) <b>Asian Office of Aerospace Research &amp; Development, (AOARD), Unit 45002, APO, AP, 96338-5002</b>				10. SPONSOR/MONITOR'S ACRONYM(S) <b>AOARD</b>	
				11. SPONSOR/MONITOR'S REPORT NUMBER(S) <b>AOARD-084019</b>	
12. DISTRIBUTION/AVAILABILITY STATEMENT <b>Approved for public release; distribution unlimited</b>					
13. SUPPLEMENTARY NOTES					
14. ABSTRACT <b>This work presents the development of an oxygen-based diode laser absorption sensor designed to be used in a supersonic combustion ramjet engine inlet. The sensor uses free-space propagation of light from a vertical-cavity surface-emitting laser (VCSEL) to determine the temperature, velocity and angle of attack of an engine inlet in hypersonic flow. The report outlines the method of calculating these parameters based upon the absorption spectrum, calibrations of the system in a gas cell, tests of operation at high temperature and tests of the sensor in a hypersonic facility flow. The system in its current form is capable of measuring both free stream temperature and velocity at measurement rates of 150 Hz. Sensitivity to vibration and very low absorption values prevented the system from being able to determine the angle of attack. It is possible that, with more attention to reducing the effect of vibration, some information about the angle of attack may be obtained.</b>					
15. SUBJECT TERMS <b>Aerospace, Hypersonic Flowfield Measurements</b>					
16. SECURITY CLASSIFICATION OF:			17. LIMITATION OF ABSTRACT <b>Same as Report (SAR)</b>	18. NUMBER OF PAGES <b>43</b>	19a. NAME OF RESPONSIBLE PERSON
a. REPORT <b>unclassified</b>	b. ABSTRACT <b>unclassified</b>	c. THIS PAGE <b>unclassified</b>			

# Contents

<b>1</b>	<b>Introduction</b>	<b>2</b>
1.1	Tuneable Diode Laser Spectrometers . . . . .	2
1.2	Absorption Measurements in High-Speed Flow . . . . .	3
<b>2</b>	<b>Optical System for Inlet Absorption Measurements</b>	<b>3</b>
<b>3</b>	<b>Theory for Inlet Temperature Measurements</b>	<b>4</b>
3.1	Flowfield Modeling . . . . .	5
3.2	Absorption Modeling . . . . .	7
3.3	Results of Inlet Modeling . . . . .	8
3.4	Effect of Noise on Parameter Fitting . . . . .	10
<b>4</b>	<b>Gas Cell Experiments</b>	<b>13</b>
4.1	Gas Cell Data Reduction . . . . .	15
4.2	Gas Cell Results . . . . .	16
<b>5</b>	<b>Thermal Modeling and Testing</b>	<b>16</b>
5.1	Heat Transfer Calculation Method . . . . .	18
5.2	Post-Shock Conditions . . . . .	19
5.3	Flat Plate Heat Fluxes . . . . .	19
5.4	Leading Edge Heat Fluxes . . . . .	21
5.5	Two-Dimensional Heat Diffusion . . . . .	22
5.6	Computation Results . . . . .	22
5.7	Typical Results . . . . .	23
5.8	Comparison with Previous Work . . . . .	24
5.9	Limitations of Heat Flux Analysis . . . . .	25
<b>6</b>	<b>High-Temperature-Operation Tests</b>	<b>26</b>
6.1	High-Temperature Test Results . . . . .	28
<b>7</b>	<b>Hypersonic Facility Tests</b>	<b>29</b>
7.1	Arrangement for Hypersonic Experiments . . . . .	29
7.2	Data analysis . . . . .	30
7.3	Temperature Measurements . . . . .	35
<b>8</b>	<b>Conclusions and Future Work</b>	<b>36</b>

## Abstract

This work presents development of an oxygen-based diode laser absorption sensor designed to be used in a supersonic combustion ramjet engine inlet. The sensor uses free-space propagation of light from a vertical-cavity surface-emitting laser (VCSEL) to determine the temperature, velocity and angle of attack of an engine inlet in hypersonic flow. The report outlines the method of calculating these parameters based upon the absorption spectrum, calibrations of the system in a gas cell, tests of operation at high temperature and tests of the sensor in a hypersonic facility flow.

The system in its current form is capable of measuring both freestream temperature and velocity at measurement rates of 150 Hz. Sensitivity to vibration and very low absorption values prevented the system from being able to determine the angle of attack. It is possible that, with more attention to reducing the effect of vibration, some information about the angle of attack may be obtained.

# 1 Introduction

The supersonic combustion ramjet engine is, at present, one of the more promising high-speed flight propulsion technologies. One of the reasons for this is the simplicity of the engine design, having no moving parts and requiring no external ignition source and the fact that scramjets do not need to provide their own oxidizer (Heiser and Pratt 1994). Despite this simplicity, several obstacles to the use of scramjet propulsion systems have become apparent, including the ability to produce sufficient fuel-air mixing at high speed, large total pressure losses, reduction in specific impulse with increasing flight Mach number and the sensitivity of combustion to inlet temperature. This last problem can be very significant. At Mach 8 and a freestream temperature of 236 K, for example, a 10-degree double-wedge inlet will have a maximum post-shock temperature of 410 K at zero angle of attack and 500 K at an angle of attack of  $3^\circ$ . Inlets with more compression stages will have even larger temperature increases.

## 1.1 Tuneable Diode Laser Spectrometers

As combustor performance is so sensitively dependent on the inlet flow conditions, it is important that measurements in the inlet should be capable of measurement in the flow itself rather than at a surface. The measurement techniques used at these hypersonic flow conditions should also be non-intrusive. Tuneable diode laser absorption spectroscopy (TDLAS) using vertical-cavity surface emitting lasers (VCSELs) is a technique that has these advantages, and a number of others that make it very well suited to measurements in scramjet inlet flows. The VCSEL is a laser that was initially designed for use in the telecommunications industry (Soda et al. 1979), but has a number of advantages for sensing applications. Like most diode lasers, it has no moving parts and has a high electrical efficiency compared with other types of lasers. The VCSEL's surface-emitting characteristic means that the cavity can be formed using traditional integrated-circuit fabrication techniques, making VCSELs small and potentially inexpensive. As the intention is to use the laser for measurements in the physically confined environment in a model scramjet inlet, the small size and lack of moving parts makes this type of laser a good choice of optical sensor.

VCSELs are also very thin in comparison to other diode laser configurations. Diode lasers modulate their frequency by changing the cavity size with applied current, and a thinner laser will have a proportionally larger cavity size variation than thicker lasers. For this reason the VCSEL can scan over a wavelength range more than 10 times wider than the distributed feedback (DFB) lasers typically used for similar applications. This means that the VCSEL can potentially scan over many transitions, while the DFB laser can usually tune over only one or two, so the VCSEL can provide more spectral information in a given scan. The VCSEL can also tune very quickly, with scans at rates of up to 5 MHz being recorded in the literature (Lackner et al. 2003). The thinness of the lasing medium also

ensures that the output radiation has a single longitudinal mode and is therefore spectrally narrow, a very desirable property for high-resolution spectroscopy. Finally, because the radiation emerges from the surface of the gain medium the expansion angle of the beam is uniform, removing the need for the aspheric collimating optics required to minimize beam expansion nonuniformity in other lasers.

## 1.2 Absorption Measurements in High-Speed Flow

Although diode lasers are only now used in hypersonic flight tests, and none of the results of flight test investigations have been published, several tests have been performed in ground-test facilities to determine the incoming flow properties and quantify the extent of combustion. These ground tests have proved particularly important for new and speculative engine designs such as pulsed detonation engines (Ma et al. 2003) and scramjet engines (Upschulte et al. 2000, Griffiths and Houwing 2005, Williams et al. 2006) although tests have also been performed on model gas turbine engines (Zhou et al. 2007). All of these TDLAS systems chosen for use in combustor ground tests have used water vapor as the absorbing species, because of the relatively large absorbances achievable using standard telecommunication diodes, which in turn allow measurements to be performed with acceptable signal-to-noise ratios. This is quite reasonable for combustor flows, where the combustion generates significant  $\text{H}_2\text{O}$ . At the flight altitudes at which scramjets operate, there is no water vapor in the air. An inlet sensor needs to use oxygen as the absorbing species, as this is the only option for absorption measurements in inlet air. Oxygen absorption lines exist in the *A*-band near 760 nm, a wavelength region that is accessible to both distributed feedback lasers and VCSELs. These lines are very weak because the transitions are spin-forbidden. In the hot, vibrating, hostile environment of a scramjet inlet in flight, it can be challenging to make measurements with a high signal-to-noise ratio given such low absorbances. Thus any measurement technique used in this environment must be resistant to amplitude noise on the absorption signal. For this reason, previous studies have made measurements in relatively high-density flows, including an unburnt fuel sensor for a model pulsed detonation engine (Sanders et al. 2000) and a post-shock temperature sensor in shock tube flows (O’Byrne et al. 2007). In this paper we theoretically test a potential TDLAS sensor for use in much lower-density flows, to determine whether it is capable of measuring freestream Mach number and angle of attack.

## 2 Optical System for Inlet Absorption Measurements

The optical system used for making the absorption measurements is shown in Fig. 1. The temperature-controlled VCSEL is tuned in wavelength by varying the current using a low-noise constant-current supply modulated by a sawtooth waveform, which varies both the intensity and the wavelength of the laser radiation. The beam from the VCSEL is collimated and passed through a calcite polarizing prism, having its plane of polarization nominally aligned with that of the VCSEL. This is done to minimize polarization variations in the laser beam, as explained in more detail in Sec. 4. A second prism splits the beam into two beams, each having half the intensity of the original beam. One of the beams is then directed onto a silicon PIN photodetector while the other is directed by a turning prism into the inlet. It passes through the duct and a second window, then is reflected by a retroreflecting corner-cube back in the direction parallel to its entry into the inlet. The reflected beam is shown in Fig. 1 displaced in the streamwise direction for clarity, but the beam is actually displaced out of the plane of the page so the path lengths of the two beams can be assumed to be identical. The reflected beam re-enters the box beneath the lower inlet plate and is detected by a second silicon photodetector. The photocurrents from the two detectors are passed to a log-ratio amplifier which produces at its output an absorbance signal,  $\log(I/I_0)$ , that can be directly compared to that calculated using Eq. 9 described in Sec. 3.2.

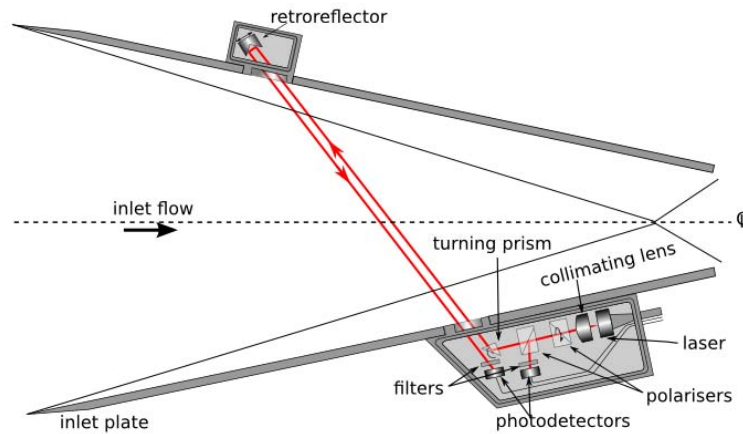


Figure 1: Schematic of TDLAS Optics.

Section 3 involves determining how well the system shown in Fig. 1 can measure the freestream Mach number and angle of attack for spectra containing noise, as the very low absorbance, the vibration and the aerodynamic heating of the vehicle can all add noise to the spectrum. Sources of noise due to optical artifacts like etalon formation or spectrum baseline drift will not be considered in this analysis.

### 3 Theory for Inlet Temperature Measurements

Using any laser-based technique in a flight test vehicle places constraints on the experimental arrangement compared with equivalent laboratory systems. Each additional component is a potential source of failure, while data bandwidth and physical space restrictions make multiple beam paths and additional wavelengths a luxury, the benefits of which need to be weighed carefully against the added complexity and space. This poses a particular problem when line-of-sight variations in flow properties need to be determined. The usual method of measuring variations along a line of sight is tomography (Villareal and Varghese 2005, Zhang et al. 2001), but this technique requires absorption spectra to be generated through several projections in different directions, and these add complexity to the system. Instead, we use a method first discussed by Sanders *et al.* (Sanders et al. 2001) and subsequently used by others (Webster et al. 2005, Liu et al. 2007) for determining line-of-sight temperature distributions in flows with simple geometries. This technique relies on measuring absorption from a number of transitions, each having different linestrength variation with temperature, to provide information that can be directly and unambiguously linked to the spatial temperature distribution. If the variation in absorbance for  $n$  absorption features can be described in terms of  $m$  parameters describing the variation in conditions along the path length, then provided  $n \gg m$ , the information in the spectrum can be used to fit the  $m$  parameters using a nonlinear least-squares technique. The flow in a simple two-wedge hypersonic inlet is a simple test for this technique, as the flowfield can be easily described analytically by assuming it contains three distinct regions: two shock layers from the two plates and the freestream flow between the two shock layers. This is an idealization of the flowfield because it does not account for the high-temperature boundary layers on each of the plates. These boundary layers, however, are thin in comparison to the flow regions and contribute very little to the total absorption signal. Because they are high-temperature regions compared with the other parts of the flowfield, they tend to absorb less than lower temperature regions for the  $A$ -band region over the same path length because the transitions tend to have low ground-state rotational energies.

Figure 2 shows temperature maps from computations of the two-plate, two-wedge inlet flow at zero angle of attack in a Mach 8 freestream at 30 km altitude. The top half of the computed flowfield

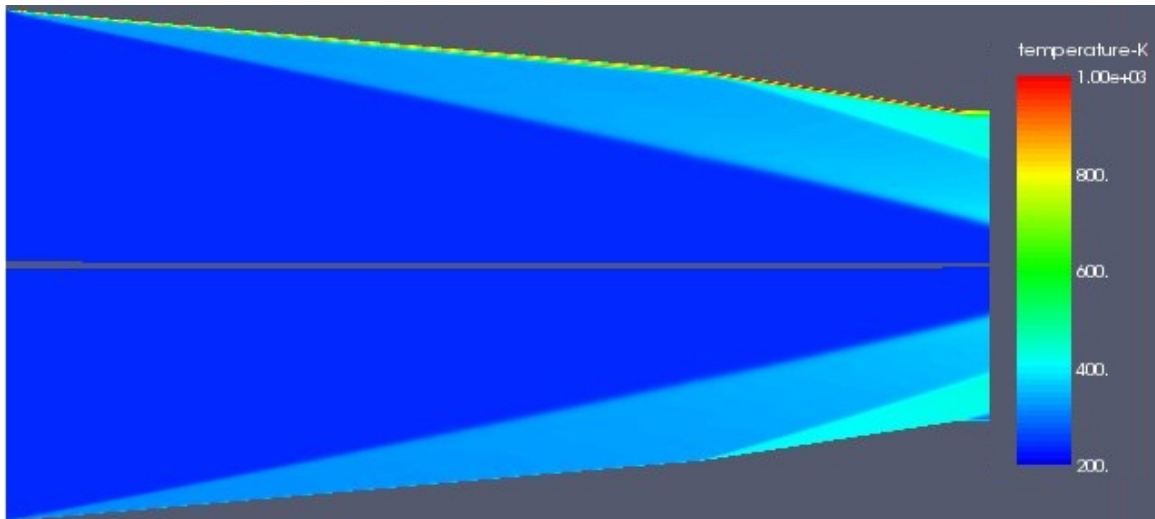


Figure 2: Computed temperature map for inlet flow at Mach 8. Upper half: laminar viscous computation. Lower half: inviscid computation. Flow is from left to right.

includes the boundary layer while the lower half of the computed flowfield assumed inviscid flow. The flowfields were calculated using the MBCNS Navier-Stokes solver (Jacobs 1998). The two shock layers, originating at the leading edges of the plates, are clearly visible in the computations. The boundary layer, shown as a high-temperature region immediately below the top plate is much thinner than either the shock layers or the freestream region, although it does visibly displace the shock wave compared with the inviscid calculation, as demonstrated by the shock wave being closer to the symmetry axis in the upper half of the image.

Ignoring the effect of the boundary layer allows us to simplify the problem by assuming two-dimensional inviscid flow in the inlet for this study. Using this assumption, the conditions in the inlet can be directly calculated using analytical shock-jump relations, allowing rapid fitting of the distributions and simple interpretation of the data. There is nothing to prevent the full viscous flowfield from being computed each time the fit parameters are varied, but such an approach would make the computation much longer without improving accuracy in fitting by more than a few percent. For cases where the inlet geometry is more complex, there is really no alternative to a full three-dimensional flowfield computation to determine temperature, velocity and angle of attack of the vehicle.

### 3.1 Flowfield Modeling

The simplified two-plate inlet used in this analysis is shown schematically in Fig. 3. The laser passes twice through the two shock layers and the freestream: it is reflected from the upper plate back down to the lower plate, as we shall see later when the optical arrangement is discussed. To determine the absorption along this path, we need to determine the temperature, number density of absorbing molecules and the component of flow velocity in the laser propagation direction, in each of those three regions. These quantities change as the freestream Mach number, the altitude and the angle of attack of the vehicle changes. Thus, the absorbance along the line of sight of the beam will be a function of only these three quantities. For this analysis we will assume that the altitude is known, and this dictates the freestream temperature and number density. We will also assume that the mole fraction of absorbing oxygen molecules is everywhere constant in the flow. Given that the post-shock temperature is well below the temperature required to dissociate oxygen, this is a good assumption.

The inlet consists of two plates, each angled at  $\theta$  from the horizontal, which can also have an additional angle of attack to the flow,  $\alpha$ , making the angle of the two plates to the freestream  $\theta \pm \alpha$ . Because the plate is angled to the flow, a shock wave will form at the leading edge of each plate, making an angle  $\beta$  to the plate, which is related to the deflection angle, the freestream Mach number

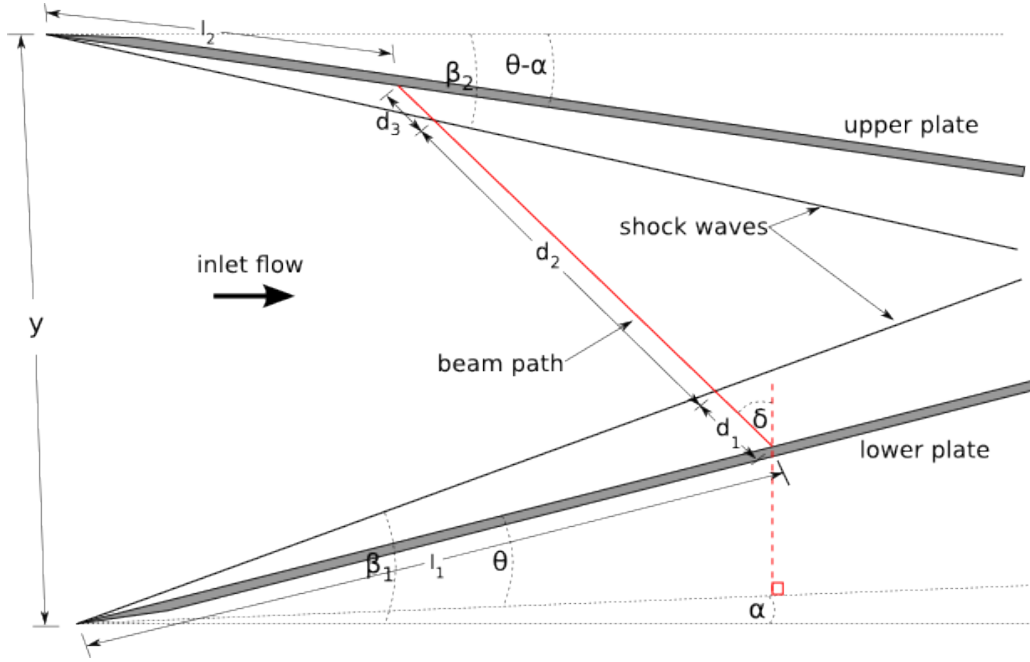


Figure 3: Simplified two-plate inlet geometry used in the analysis.

$M_\infty$  and the ratio of specific heats  $\gamma$  through the equation (Anderson 1990)

$$\tan(\theta \pm \alpha) = 2 \cot \beta \left[ \frac{M_\infty^2 \sin^2 \beta - 1}{M_\infty^2 (\gamma + \cos 2\beta) + 2} \right] \quad (1)$$

The shock angle  $\beta$  can be solved for iteratively in Eq. 1, if the deflection angle  $\theta \pm \alpha$  and the freestream Mach number  $M_\infty$  are known. The post-shock temperature, pressure and velocity are then computed using the standard normal shock relations (Anderson 1990) once the value of  $\beta$  has been determined for each plate and using the component of the freestream Mach number normal to the shock wave,  $M_{n,\infty} = M_\infty \sin \beta$ :

$$\frac{p_d}{p_\infty} = 1 + \frac{2\gamma}{\gamma + 1} (M_{n,\infty}^2 - 1) \quad (2)$$

$$\frac{T_d}{T_\infty} = \frac{p_d}{p_\infty} \frac{(\gamma - 1)M_{n,\infty}^2 + 2}{(\gamma + 1)M_{n,\infty}^2} \quad (3)$$

$$u_d = \frac{\sqrt{M_{n,\infty}^2 + [2/(\gamma - 1)]}}{\sin(\beta - (\theta \pm \alpha)) \sqrt{[2\gamma/(\gamma - 1)]M_{n,\infty}^2 - 1}} \sqrt{\gamma R T_d} \quad (4)$$

where the subscripts  $\infty$  and  $d$  indicate conditions upstream and downstream of the shock wave respectively, and  $R = 287 \text{ J kg}^{-1} \text{ K}^{-1}$  is the specific gas constant of air. The deflection angle is  $\theta + \alpha$  for the lower plate and  $\theta - \alpha$  for the upper plate.  $\beta$  is measured relative to the freestream direction for both shock waves. Once the shock angle is known, the path lengths of the laser beam through the three flow regions can be determined. If the vertical distance between the tips of the inlet plates is given by  $y$ , the length downstream of the tip along the plate surface at which the beam enters the inlet is  $l_1$ , and  $\delta$  is measured relative to  $\theta$  as shown in Fig. 3, then the beam reaches the upper plate at a distance  $l_2$  from the tip, where

$$l_2 = l_1 - \frac{(y - 2l_1 \sin \theta) \sin \delta}{\cos(\theta + \delta)} \quad (5)$$



The laser propagation distances through the first shock layer ( $d_1$ ), the second shock layer ( $d_3$ ) and the freestream ( $d_2$ ) are

$$d_1 = l_2 \frac{\sin(\beta_2 - (\theta - \alpha))}{\cos(\alpha + \beta_2 + \delta)} \quad (6)$$

$$d_3 = l_1 \frac{\sin(\beta_1 - (\theta + \alpha))}{\cos(\beta_1 - (\delta + \alpha))} \quad (7)$$

$$d_2 = \frac{(y - 2l_1 \sin \theta) \cos \theta}{(\cos(\delta + \theta))} - (d_1 + d_3) \quad (8)$$

respectively, where  $\beta_1$  and  $\beta_2$  are the angles from the horizontal of the first and second shock waves the laser passes through in going from the lower plate to the upper plate.

Once the path lengths and flow conditions in each region have been computed, the absorption spectrum for a given angle of attack and freestream Mach number can be calculated. Each of the distances  $d_1$ ,  $d_2$  and  $d_3$  is doubled, as the beam is retroreflected from the top plate back to the bottom plate before detection, as we discuss later.

### 3.2 Absorption Modeling

A laser beam passing through a medium having uniform conditions over a path length  $L$  will be absorbed at the resonance frequency  $\nu$  of a molecule according to the Beer-Lambert law (Measures 1988)

$$\kappa(\nu)z = \ln(I_0/I) = 2.303 \log(I_0/I) \quad (9)$$

where  $\kappa(\nu)$  [ $\text{cm}^2 \text{ molecule}^{-1}$ ] is the absorption coefficient and  $z$  [ $\text{molecule cm}^{-3} \text{ cm}$ ] is the optical density or the number per unit area of molecules along the line of laser propagation.  $I_0$  and  $I$  [ $\text{W cm}^{-2}$ ] are the intensities at the beginning and end of the region, and the base-10 logarithm of  $I/I_0$  is known as the absorbance. The absorption coefficient is defined in terms of a linestrength  $S$  [ $\text{cm molecule}^{-1}$ ] according to

$$S = \int_{-\infty}^{\infty} \kappa(\nu) d\nu \quad (10)$$

and the integral can be isolated in terms of the transition lineshape  $g(\nu - \nu_0)$ , giving

$$\kappa(\nu) = Sg(\nu - \nu_0) \quad (11)$$

Now  $g$  is a generic lineshape function whose shape is a function of the pressure, temperature and composition of the gas. The profile function chosen in this study is the Voigt profile (Measures 1988), calculated using the method of Humlíček (Humlíček 1982). By definition, for any given line shape,  $g$  is normalized such that

$$\int_{-\infty}^{\infty} g(\nu - \nu_0) d\nu = 1 \quad (12)$$

The linestrength  $S$  is a function of the temperature of the gas and of the particular absorption transition, as defined by

$$S(T) = S(T_0) \frac{Q(T_0)}{Q(T)} \exp \left[ \frac{hcE}{kT} \left( \frac{1}{T} - \frac{1}{T_0} \right) \right] \quad (13)$$

where  $Q(T)$  is the partition function of the absorbing molecule at temperature  $T$ ,  $T_0 = 296$  K is a reference temperature and  $E$  is the ground-state energy. For these calculations, the HITRAN 2004 molecular database (Rothman et al. 2005) was used to calculate both  $S(T_0)$  and  $Q(T)/Q(T_0)$ .

Because the inlet flow moves at high speed, the spectral absorption wavelengths are Doppler-shifted by an amount proportional to the component of the velocity in each region in the direction of laser beam propagation, *i.e.*

$$\Delta\nu_D = \frac{u}{c} \nu_0 \cos \psi \quad (14)$$

where  $\psi$  is the angle between the flow and the beam path. It is this relation that gives the absorption measurement its sensitivity to flow velocity, as the beam traverses the inlet in two opposite directions.

The method for fitting the Mach number and angle of attack for a given spectrum is as follows. A ‘measured’  $(M_\infty, \alpha)$  condition at 30 km altitude was chosen as a simulated experimental spectrum to be fitted. An initial guess for a Mach number between 4 and 12 and an angle of attack between -6 and 6 degrees was chosen. The shock wave angles were solved iteratively for these guessed values using Eq. 1. Once the angles were known, the post-shock conditions were computed using Eqs. 2–4 and the path lengths were computed using Eqs. 6–8. For each of these three paths, the lineshape function was computed and the temperatures used to determine the linestrength through Eq. 13 for all the *A*-band transitions between 760.5 and 761.5 nm. This region was chosen because a previous computational study of the *A*-band transitions showed that this part of the spectrum was the most sensitive to temperature variations in the flow between 250 and 1250 K (Webster et al. 2005). The line locations in HITRAN were shifted from  $\nu_0$  to  $\nu_0 + \Delta\nu_D$  in each of the three flow regions using Eq. 14.

Once the linestrengths and lineshapes had been determined, the absorption coefficient was calculated using Eq. 11 and this in turn determined the absorbance from Eq. 9. The absorbance from each of the three regions was used twice, with the second beam Doppler-shifted in the opposite direction, to account for double-passing through the inlet. The two sets of three absorbances were then summed to generate a final spectrum. This guessed spectrum was compared to the ‘measured’ spectrum and the least-squares difference between the two spectra was summed over the wavelength range. This function value was used as the fitting parameter to be minimized by varying  $(M_\infty, \alpha)$ , using values selected by a Levenberg-Marquardt nonlinear least-squares fitting routine. The least-squares minimum was taken to correspond to the correct fitted parameters. As there were 8 transitions over this spectral range and two fitted parameters, there was sufficient spectral information to fit for both Mach number and angle of attack.

### 3.3 Results of Inlet Modeling

Figure 4 shows the calculation of a spectrum at a baseline condition comprising Mach 8 flow at 30 km altitude and an angle of attack  $\alpha$  of  $2^\circ$  to the freestream direction. The inlet consists of two plates at  $\theta = 10^\circ$ , with  $y = 0.2$  m and  $l_1 = 0.2$  m. The angle  $\delta$  was  $45^\circ$ .

The 8 transitions are clearly visible in Fig. 4, as 8 pairs of Doppler-shifted transitions arising from the spectra of the incoming and return beams. As the return beam is retroreflected parallel to the incoming beam, then the frequency separation between the two beams is twice the Doppler shift. At Mach 8, the Doppler shift is sufficient to completely separate the absorption profiles arising from the incoming and reflected beams. The peak absorbance in Fig. 4 is less than  $6 \times 10^{-4}$ , which is very weak, but still large enough to be realistically detectable using low-noise detection techniques such as wavelength modulation or log-ratio detection, which both have been shown to have practical absorbance detection limits below  $10^{-5}$  (Pavone and Inguscio 1992, Allen et al. 1995). The transitions are also very narrow, which means that the detection system must sample a large number of points. For the data presented here, each spectrum consists of 10 000 data points. One important feature of the  $O_2$  spectrum in this region is the large spectral separation between the effectively isolated spectral

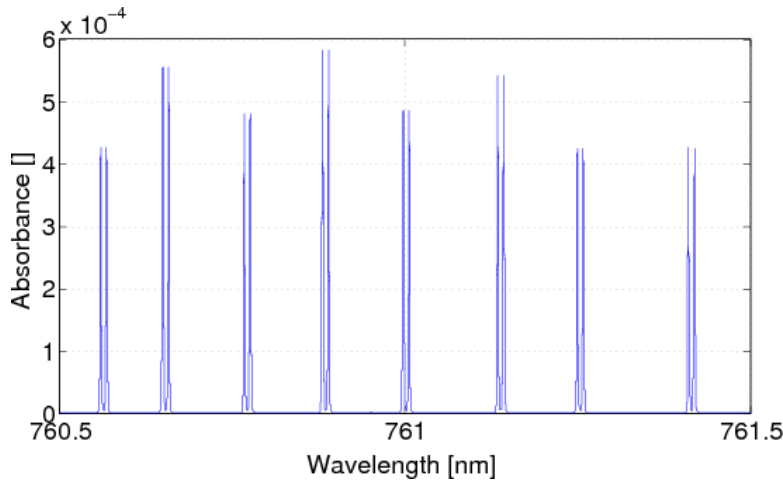


Figure 4: Baseline spectrum for a Mach 8 flow at  $2^\circ$  angle of attack.

lines. This separation is important because it provides plenty of room for absorption features to be Doppler-shifted without interfering with neighboring transitions, which can complicate the spectral fitting process.

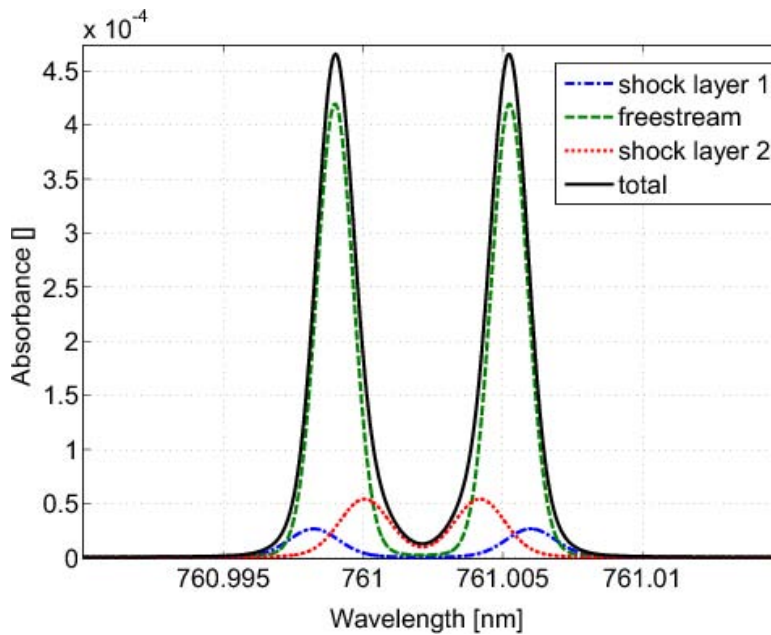


Figure 5: Contributions to absorbance from three flow regions, and summed absorbance for Mach 8,  $\alpha = 0^\circ$ ,  $\delta = 30^\circ$ .

Figure 5 shows one of the Doppler-shifted line pairs from Fig. 4, including the contributions from absorption in each of the three flow regions. The largest absorption signal occurs in the freestream, both because the linestrength is higher in the colder flow, and because the path length is much longer than that of the two shock layers. Because the signal from each of the shock layers is smaller than that from the freestream, and because there is a significant Doppler shift between the signals in the shock layers and the freestream, this technique can determine the freestream Mach number very precisely. It is also apparent from Fig. 5 that the absorption signal from the two shock layers is spectrally broader than that from the freestream, because the temperature and pressure in both of these regions is higher.

The sensitivity of the system to Mach number can be seen in Fig. 6, which contains images of one of the *A*-band transitions for Mach numbers of 8, 9 and 10. The spreading apart of the absorption features caused by the incoming and outgoing beams is easily discerned and linearly related to the

velocity. The increasing Mach number also causes the peak absorbance to drop slightly as the flow in the two shock layers becomes hotter.

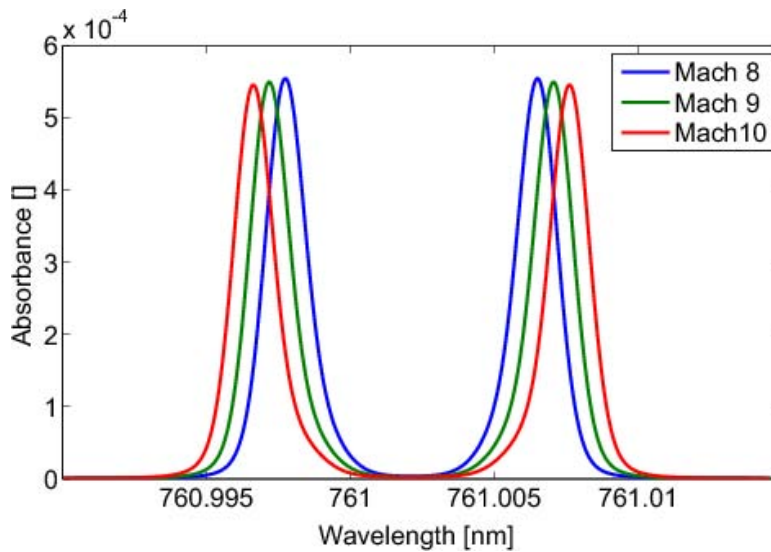


Figure 6: Spectra for varying Mach numbers,  $\alpha = 0$ .

Because the freestream peak dominates Fig. 5, the sensitivity to angle of attack comes mostly from the location of the absorption components from the two shock layers, as the freestream temperature, and therefore its effect on the absorption spectrum, is the same for all three flows. As the inlet tilts, the shock layer becomes thicker at the bottom and the flow becomes hotter, while the upper shock layer becomes relatively thinner and cooler. The asymmetry in the two path lengths through the shock layer flows means that there is sensitivity to the angle of attack, though the effect itself may be difficult to measure because the change in signal is relatively small compared with the freestream absorption, and is partially obscured by that signal.

The effect on the spectral lines caused by changes in the angle of attack at Mach 8 conditions is shown in Fig. 7. In this plot, spectra for angles of attack of  $-3^\circ$ ,  $0^\circ$  and  $3^\circ$  are shown. Comparison of this plot with Fig. 6 shows that the two variables have a similar effect on the spectrum. There are, however, some differences between the two effects that can allow the least-squares fitting code to differentiate between them. In Fig. 6, the region between the two peaks does not change its shape with increasing Mach number: only the distance between the peaks changes. In Fig. 7, the region of the spectrum between the two peaks changes its shape, again because of the effect of the changing shock layer thickness on the flow. The gradient of the inner portion of the spectral line becomes more vertical as the angle of attack is reduced.

In addition to the effect of Mach number and angle of attack on individual transition features, further differentiation occurs due to the different temperature sensitivities for different transitions, and different lower-state energy levels of the transitions. This manifests as a variation in relative peak heights for the eight absorption peaks as each variable changes.

### 3.4 Effect of Noise on Parameter Fitting

When the spectrum is free from noise, it is straightforward to fit a spectrum for the Mach number and angle of attack. In a flight test, the signal is likely to have significant random noise caused by vibration and the small absorbance, as well as sources of systematic noise from time-varying etalon signals and extraneous light from the sun and from combustor flow luminosity. To some extent the systematic variations can be minimized by careful optical design, subtracting the time-varying portion of the background signal fitted using a polynomial and by using wavelength-selective filters near the detectors. We were interested in knowing the extent of the effect of high-frequency Gaussian noise

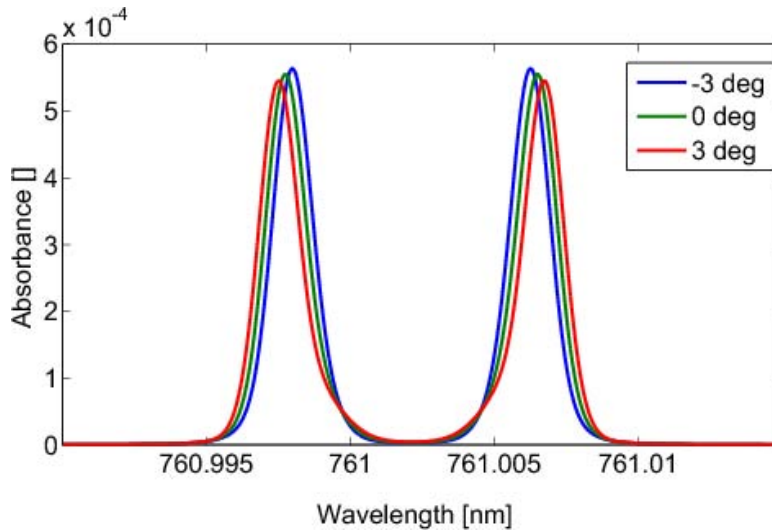


Figure 7: Spectra for varying angles of attack,  $M_\infty = 8$ .

on the fitting of the absorption signal. To simulate this, we added random noise with an average relative value compared with the largest peak absorbance of between 0 and 50 %. This noise was added to the signal for the ‘measured’ condition of Mach 8 freestream flow and  $\alpha = 2^\circ$ . Ten random initial guess conditions were chosen with Mach numbers between 4 and 12 and with angles of attack between  $-6$  and  $6^\circ$ . The fitting routine was then used to fit for either Mach number or angle of attack, with the non-fitted value assumed known. Figure 8 is an example of one such noisy spectrum and the spectrum fitted for Mach number to the two transitions. The ‘measured’ spectrum had 20 % noise added to it before fitting. It is clear that even though the noise is significant, the routine was able to fit the Mach number well. The fit is so good because of the accuracy of the freestream Doppler shift measurement: the retroreflector guarantees that the beam returns at the same angle it entered with, so that the separation between the two transitions is a function only of the Doppler shift and does not depend on measurement of some external reference velocity. The noise has minimal effect on the Mach number prediction because this depends on the location of the peak rather than its amplitude.

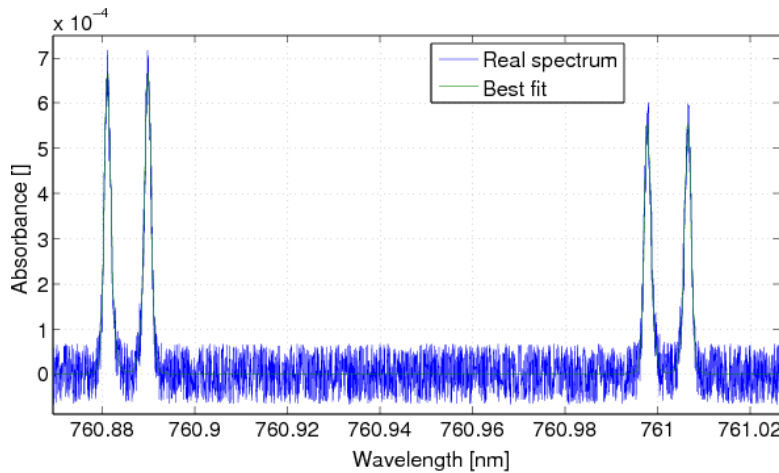


Figure 8: Fitted spectrum to ‘measured’ spectrum with 20 % noise added:  $\alpha = 0$ ,  $M_\infty = 8$ .

Spectrum-fitting simulations were performed with different levels of noise, assuming that the angle of attack is known and the Mach number unknown. The results of these tests are summarized in Fig. 9. The points on the plot are the average for 10 fits from different randomized initial guesses, and were within  $\pm 0.02$  of 8, even for spectra with noise up to 50 % of the signal amplitude. This shows the robustness of the Mach number fit in the routine.

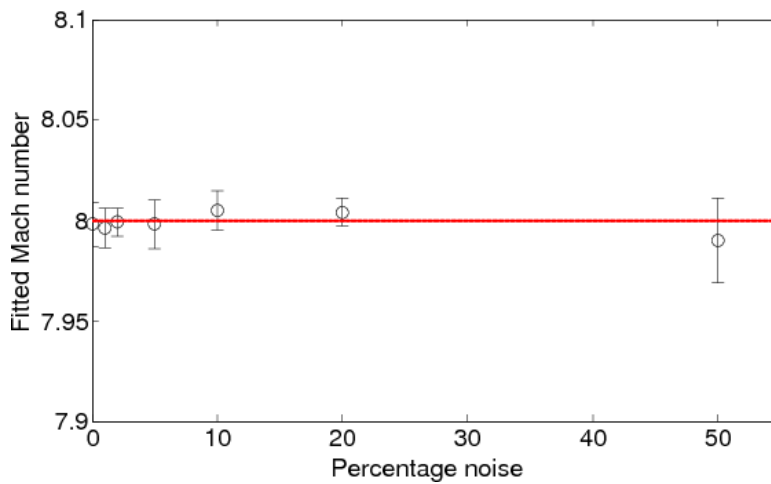


Figure 9: Sensitivity of Mach number fit to noise intensity.

Figure 10 shows the results of fitting for angle of attack assuming the correct Mach number for the simulation. Two interesting facts are apparent from these results. First, the uncertainty in the angle of attack does not depend strongly upon the signal-to-noise ratio of the absorption signal, as the error bars are not correlated with the percentage noise. The second interesting feature of Fig. 10 is the fact that the angle of attack has been consistently under-predicted by approximately  $0.25^\circ$  for all ‘measured’ spectra. This is true even for the case where there is no additional noise on the spectrum. This is related to the fitting routine tending to find a local minimum in the least-squares residual if the initial guess approached the solution from below, whereas those fits generated from an initial guess at a higher angle of attack tended to approach a global minimum corresponding to the correct angle of attack. This indicates that a more robust fitting algorithm that starts at a number of initial guesses and takes the true least-squares minimum may give a better evaluation of the angle of attack.

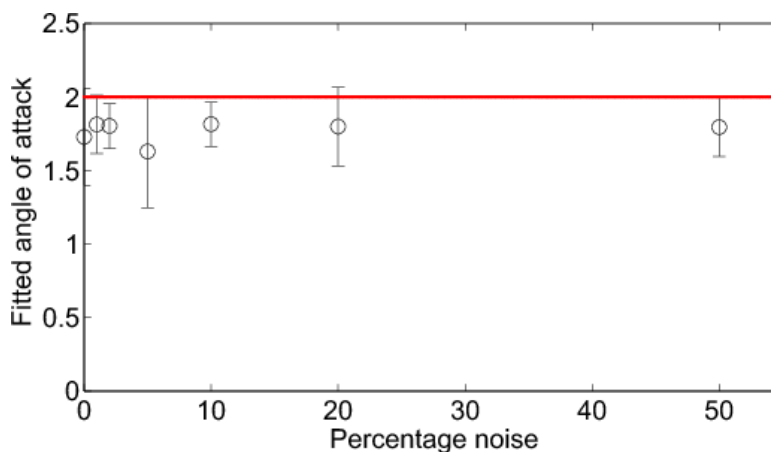


Figure 10: Sensitivity of angle of attack fit to noise intensity.

It should be noted that setting both the Mach number and the angle of attack as free variables did not significantly change the fitted angle of attack when compared with Fig. 10. This is because the Mach number is so strongly correlated to the distance between the highest-amplitude peaks for each absorption line.



## 4 Gas Cell Experiments

A scramjet traveling at Mach 8 and 30 km altitude has a freestream temperature of 225 K and post-shock temperatures of up to 600 K. The Ludwig tube tests presented in Sec. 7 had a freestream temperature of approximately 65 K. Knowing the linestrength and its variation with temperature is very important to the precision of the temperature measurements. Equation 13 shows how the linestrength scales with temperature, and requires the variation of linestrength with temperature to be known if an accurate temperature measurement is to be made. While we do not have the facilities to test the absorbance at very low temperatures, we were able to test the upper range of temperatures, between room temperature and 873 K. A more detailed description of this work can be found in the Diploma thesis of Hohmann (Hohmann 2008).

Despite the importance of oxygen measurements in flames and in high-temperature, high-speed flows, there have not been many experimental studies measuring oxygen linestrength at elevated temperatures. Nearly all of the experimental studies performed before now have been at room temperature, using relations like Eq. 13 to extrapolate to higher temperatures. Ritter and Wilkerson (1987) has measured oxygen linestrength to within 2 % at room temperature, using a multi-pass cell and a narrowband dye laser. Brown and Plymate (2000) measured the linestrengths of the *A*-branch transitions between 200 and 300 K, along with widths and pressure shifts. Robichaud et al. (2008) measured line intensities, self- and air-broadened linewidths, pressure-induced shifts, and collisional narrowing coefficients for transitions in the *P* branch using cavity ring-down spectroscopy.

To examine the effect of temperature on linestrength in the *A* band, we have performed calibration experiments in a heated gas cell. The R9R9 transition at  $13144.54\text{ cm}^{-1}$  was investigated. At 296 K this transition has a linestrength of  $7.408 \times 10^{24}\text{ cm}^{-1}/(\text{molecule cm}^{-2})$  and a pressure shift co-efficient of  $-0.0062\text{ cm}^{-1}\text{ atm}^{-1}$ , according to the HITRAN database. This particular transition was chosen because of the high strength ensuring strong signal even at low pressures and high temperatures.

The setup for the experiments is shown in Fig. 11. Temperature and current controllers are used to set the wavelength of the laser and tune across the transition. The current controller is driven by a triangular waveform from a signal generator. The laser output passes through a collimator to make it exit as a parallel beam, and then through a polarizer, which selects a single polarization plane. VCSELs can rotate their plane of polarization randomly over time, and this causes a change in the splitting ratio of the polarizing beamsplitter. Any change in splitting ratio will manifest as a modulation in the output signal of a log-ratio detector, similar to an etalon. Placing this first polarizer in the beam path converts the laser's modulation of the polarization plane into an intensity modulation, which is split evenly into two beams by the Wollaston prism. The Wollaston prism is also useful as a beamsplitter because the output beam paths are not normal to the beam, minimizing the likelihood of etalon production. One of the two output beams acts as a reference signal, passing through three mirrors with one acting to change the path length of the beam. The other beam passes through the high-temperature gas cell to a second detector.

The experiment is set up by evacuating the gas cell with the heater on and then changing the path length of the reference beam until the log-ratio signal cancels out. This ensures that the oxygen signals in the two paths cancel before the experiment. Making sure that signal from laboratory air is canceled is important because even small path differences can be significant. At room temperature the absorbance can change by 5 % between a path length of 0.17 and 0.18 m. Once the path difference has been minimized, air is then introduced into the cell and the absorption measured. It should be noted that at these high temperatures, the paths can never completely cancel because the air outside the furnace is hotter than the air in the reference path, and therefore has a slightly wider absorption profile than the reference beam. For example, outside the end of the gas cell, the ambient temperature was 303 K at a furnace temperature of 573 K, 307 K at 673 K furnace temperature and 312 K at 773 K. Later attempts were made to purge the region around the cell with nitrogen, but these did not produce significantly better signal cancelation than the method described here.

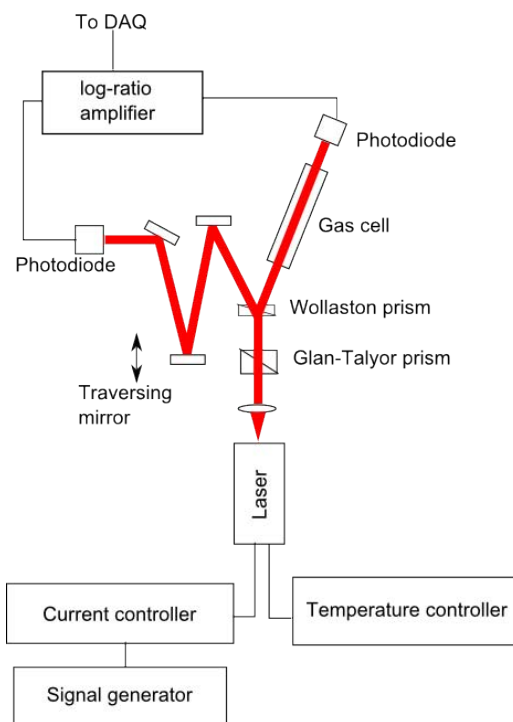


Figure 11: Schematic of the experimental setup for gas cell experiments

The gas cell is shown in Fig. 12. It fits into a Carbolite MTF 12/38/250 tube furnace. The cell is fabricated from quartz, with brass caps sealing the two ends of the cell. The windows of the cell have two fused silica rods cemented to them, to limit the air path inside the cell to the 100-mm uniform-temperature part of the furnace. The end of the silica tube was polished at an angle of three degrees, to remove etalons from the absorption signal. The amplifier was calibrated electrically by putting currents of various ratios into the two inputs of the log102 circuit. This is necessary for linestrength measurements, as the absolute value of the log ratio signal must be used. The gain of the log-ratio circuit was measured to be  $0.0162 \pm 0.0005 \text{ V}^{-1}$ . A separate optical calibration to a calibrated laser power meter produced a gain of  $0.0153 \pm 0.0039 \text{ V}^{-1}$ . The electronic calibration was used in preference to the optical calibration because of its lower uncertainty.

Wavelength of the laser was calibrated by measuring absorption at low pressure and room temperature conditions, using a wide tuning range that spanned 7 transitions. The current at which the transitions had a peak was correlated with the peak wavelength location of the transition as determined by the HITRAN database. A fourth-order polynomial was then fitted between the wavelength and the diode current for a variety of diode temperature values. Although not as precise as using an etalon for the wavelength measurement, this method is adequate for a linestrength or pressure-shift measurement, and information about broadening coefficients was not sought.

Measurements were performed initially at 296 K. The path length in the cell, although nominally 0.1 m, could not be measured precisely, and changes by a small amount every time the cell is disassembled. Therefore the HITRAN linestrength was assumed correct at 296 K and the absorption measurement was used to determine the cell path length, which was then used for all of the higher-temperature linestrength measurements. This is a reasonable assumption, as high-precision room-temperature measurements form the basis for the HITRAN database values. The path length used for all the gas cell measurements discussed here was  $0.1016 \pm 0.05 \text{ m}$ .

Measurements were obtained using spectroscopically pure dry air at nominal temperatures of 473, 573, 673 and 773 K (200, 300, 400 and 500 °C), as determined by the internal thermocouple in the furnace. At each of these temperatures, a second K-type thermocouple was traversed through the cell to ensure that the uniform-temperature region was greater than the region between the ends of the two



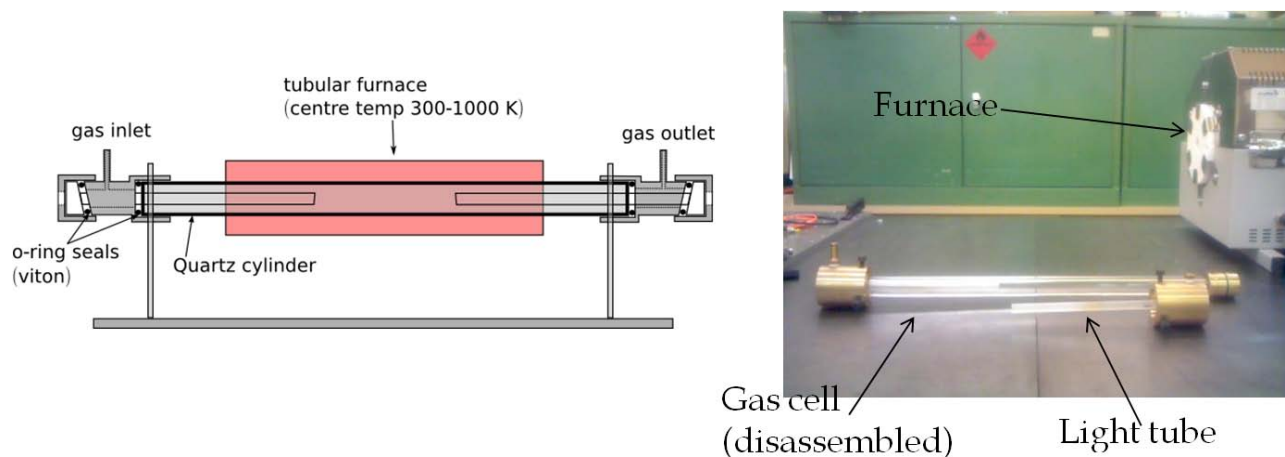


Figure 12: The high-temperature gas cell

silica rods and to determine the actual temperature in the center of the cell. Often the actual temperature was a few Kelvins below the nominal temperature setting for the furnace. All measurements were performed at atmospheric pressure. Although it is more precise to make measurements at low pressures where the lineshape can be approximated by a Doppler profile, the 0.1-m path length in the cell was too small to get a high signal-to-noise ratio at these low pressures. Also, operation at ambient pressure means that leakage of air is less likely to occur over the duration of the experiment. A Voigt profile was used to model the line shape for the linestrength determination.

The furnace was allowed to run for 30 minutes before measurements were made, to ensure that the system had reached a stable temperature. The temperature stability was ensured using both thermocouple measurements and the size of the absorption line.

#### 4.1 Gas Cell Data Reduction

A LabView program was used to acquire the signal from the log-ratio detector, via a 10-megasample-per-second analogue to digital converter. An algorithm was developed to remove the peaks from a spectrum and the remainder of the spectrum was used to fit the background using a polynomial. The fitted background was subtracted from the original spectrum to remove any residual modulation in the background signal. The spectrum was then fitted to the measured wavelength calibration with diode current.

Each spectrum was compared with the result of a spectrum generated using the HITRAN2004 database and the GENSPECT line-calculating algorithm (Quine and Drummond 2002). Temperature, pressure and path length (the latter obtained from the 296-K measurements) were treated as known quantities while the linestrength of the transition at the cell temperature was allowed to vary in Eq. 13. The partition function values and lower state energies were also taken from the HITRAN2004 database values. Individual spectra were fitted for linestrength and the linestrengths averaged, rather than averaging the spectra and fitting a linestrength. This was because the line position could move slightly over several spectra and if these were averaged the averaged spectral line would be systematically wider than the individual traces. Each measurement consisted of at least 10 spectra and for each temperature at least five separate measurements were made with the gas cell re-filled for each measurement. No significant systematic error was noted between measurements, except in cases where etalons interfered with the precision of the measurement.

A Levenberg-Marquardt nonlinear least-squares fitting algorithm was used to fit the modified experimental data against the model evaluated at the same wavenumber locations as the experiment, with the sum of the squares of the residual as the objective function to be minimized.

## 4.2 Gas Cell Results

Figure 13 shows an experimental transition at a nominal temperature of 673 K (actual temperature 668.4 K) and the fitted curve at the same conditions. At all temperatures there was a good fit between the computed and measured spectra. Each temperature had at least five separate measurements, each composed of at least 10 spectra.

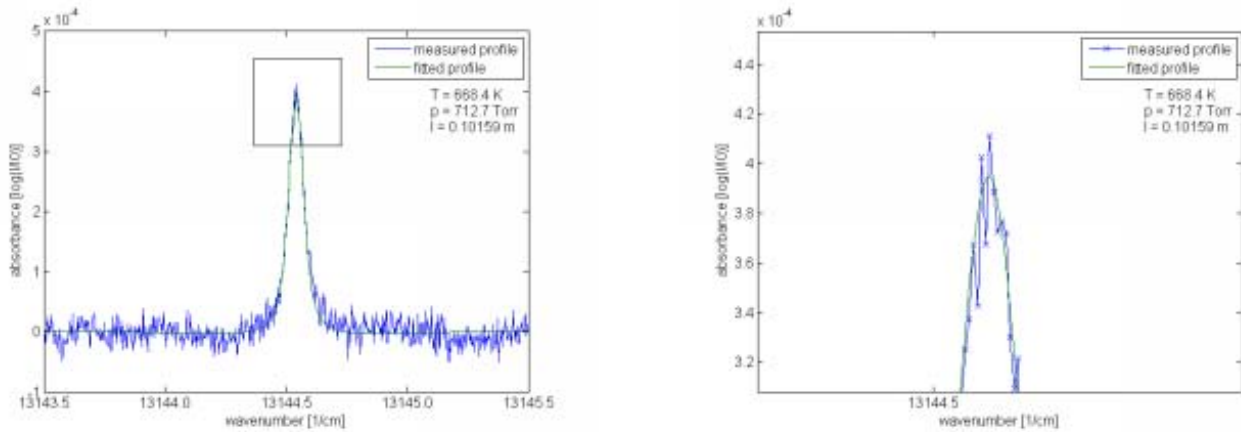


Figure 13: Experimental and fitted high-temperature spectra.

Figure 14 compares the measured linestrength of the R9R9 transition with the HITRAN values for the measured temperature values. The uncertainties on the experimental data points show the maximum of the standard deviation in the fits to individual spectra for each experiment and the standard deviation between the experiments.

It is clear from the comparison that the experimental linestrengths are higher than the HITRAN values for the two lower temperatures and lower than the HITRAN values for the two higher temperatures. The discrepancies are slightly greater than the error bars, but the measured linestrengths are within 4 % of the calculated values across the range of temperatures in the measurements.

Although the experimental and calculated linestrengths are close enough to be consistent, there is a possible reason for the variation in the difference with temperature. As mentioned previously, the temperature of the air outside the gas cell increases as the temperature in the furnace increases. If the signal path has a higher temperature than the reference path, the absorbance on the signal path will decrease, reducing the apparent linestrength. This effect increases as the temperature increases.

Despite the possible systematic error, the linestrengths agree with HITRAN to within 4 % over the range of temperatures expected in the shock layer during a flight test. This indicates that using HITRAN linestrengths would produce an acceptable temperature over the entire range of possible temperatures in an inlet measurement.

## 5 Thermal Modeling and Testing

For the sensor described in Section 2 to be suitable for use in a flight test, we need to know what thermal loads are to be experienced by the optical system and whether our chosen optical and electronic components will be able to function under those conditions, and these questions form the basis of discussion in this section and the next. In this section we discuss the heat flux into the inlet plates at the expected freestream conditions for a flight test. The importance of this heat transfer analysis is brought into relief by considering the narrow operating temperature ranges of the optical components. The operating temperature range for the lower component box, inside the leading edge, must be between 0 and 60°C as these are the operational limits of the vertical cavity surface-emitting laser

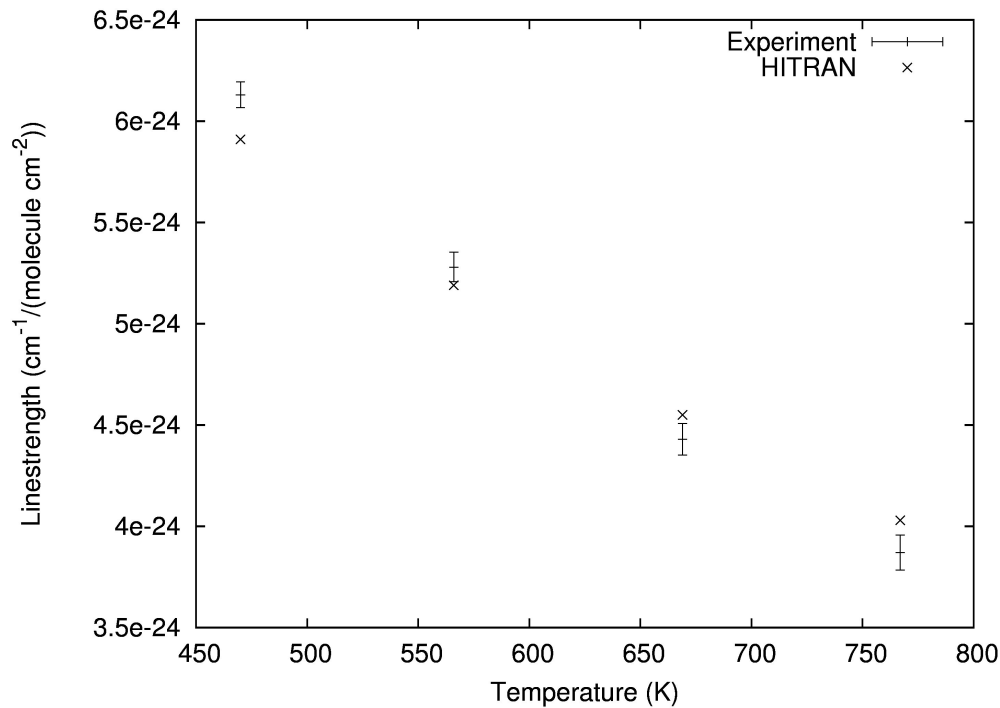


Figure 14: Comparison of measured linestrength with HITRAN linestrengths.

(VCSEL), which is the most restrictive set of temperature limits of the components. For the components mounted in the cowl, the temperature limits are that of the retro-reflector, -40 to 60°C.

The generic single-ramp scramjet inlet and flight paths used in this analysis are chosen to be as simple as possible while still a realistic estimate of the conditions that might be expected in a real flight test, and are for a generic flight path loosely based upon the ballistic trajectory of the HyShot 2 flight test, documented in Smart et al. (2006). The high velocities associated with scramjet flight tests cause the heating conditions to be severe compared to the flight conditions experienced by today's conventional air-breathing aircraft engines. Air temperatures at the leading edge stagnation point of a scramjet inlet may be greater than 3000 K, beyond the melting point of common aerospace materials. Typically, scramjets are restricted to flying at high altitudes due to the high heating effects at lower altitudes. However, there is insufficient oxygen at very high altitudes for operation of air-breathing engines. Therefore, scramjet flight must occur in a narrow band of altitudes where both high combustion efficiency and tolerable thermal loading can be achieved.

Previous thermal-structural studies of generic scramjet inlets have been conducted by Odam et al. (2005) and by Ho and Paull (2006). Odam et al. (2005) used a similar analytical solution to the one presented here to establish the heat transfer boundary conditions at the wall. A commercial finite-element code was then used to predict the temperature history of the inlet structure. We expand upon that work by incorporating variations in Prandtl number along the flow direction into the analytical solution. Ho and Paull (2006) used a constant wall temperature in the calculations of heat fluxes, while we update the wall temperature at each time-step of the calculation. Both of these studies were performed to compute heat loads during specific flight tests. Our work differs from these studies in that we have written a computational design tool that, while maintaining simplicity, allows us to quickly compute the time-accurate and spatially varying inlet heating that would be experienced by our optical system under various flight conditions.

In order to accurately predict the heat transferred through the ramp, a finite element analysis using both temporally and spatially varying boundary conditions would need to be used. Most finite element computer programs such as ANSYS are unable to model temporally and spatially varying boundary conditions without coding of complex add-on routines. Instead, we have written a simple finite-

element heat flux code that incorporates both temporally and spatially varying boundary conditions, using MATLAB.

Possible methods for the calculation of heat fluxes between the hypersonic boundary layer flow and the inlet plate surface include computational fluid dynamics (CFD) and the use of generalized analytical heat flux correlations. For initial design purposes, the use of computational fluid dynamics to predict heat fluxes is inappropriate due to the computational expense of calculating the flowfield, which would need to be computed at either a number of discrete points in the trajectory or in a time-accurate manner for the duration of the flight test. Generalized equations offer a quicker method of calculating heat fluxes for hypersonic flow over simple geometries like the one investigated here, although they are less accurate than CFD due to the assumptions made in their development. This lower level of accuracy is tolerable in the design development process as only reasonable estimates to the flow conditions are required to determine the heat flux to the plate. In 1955, Eckert proposed a series of simplified equations to predict the heat transfer for two-dimensional laminar and turbulent boundary layers up to Mach 20 (Eckert 1955). These equations were claimed to give values to within a few percent of true boundary layer calculations. We will use these equations to calculate the flowfield.

## 5.1 Heat Transfer Calculation Method

An explicit time-stepping finite-element code incorporating temporally and spatially varying boundary conditions has been developed for this study. The convective heat fluxes from the hypersonic boundary layer to the plate are calculated using generalized two-dimensional equations. The finite-element mesh of the inlet plate is generated within the code and represents the leading edge wedge and flat plate of the first inlet ramp, as shown in Fig. 15. The plate used for this study has a length of 1 m and a thickness of 10 mm. The meshing scheme used an inter-node spacing of 1 mm in both directions, so a total of 11011 nodes were used to model the plate. The leading-edge wedge nodes were distributed within the wedge at the same x-axis spacing of 1 mm, but the y-axis spacing reduced linearly with the plate thickness to fit into the wedge. The leading edge has a radius of 2 mm, so the node spacing at the leading edge is 0.2 mm. The plate is set at an angle of  $5^\circ$  incidence to the freestream. The code presented here was run using the appropriate thermal properties for both 6061-T6 aluminium and AISI 1025 steel, to see the heat transfer behavior of these two materials.

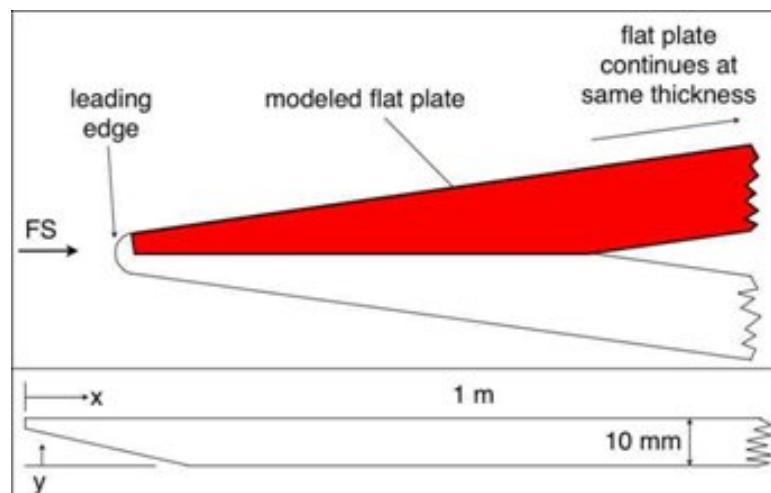


Figure 15: Plate model for heat flux calculations.

The location of the optical components box is assumed to be approximately 400 mm from the leading edge on the underside of the plate. To generate an estimate of the component box temperature, it was assumed for a worst case that the temperature of the components in the box is the same as the temperature at the underside of the plate at the mounting location. This allows the heat transfer

through the complex geometry of the component mounts and component box to be ignored. Realistically, the temperature within the components box will be less than the temperature of the chosen location, acting as a safety margin for the design.

To accurately incorporate temporally and spatially varying boundary conditions in the heat transfer analysis, the freestream conditions needed to be calculated at different times during the flight test. These conditions were calculated using the 1976 US international standard atmosphere (ISA) and the equation of state for air. The flight path used in this analysis was an ex-atmospheric ballistic trajectory similar to that of the HyShot 2 test. The heat transfer analysis is conducted between 63 km and 23 km altitude. The higher altitude was chosen for the start of the analysis as this is when aerodynamic heating effects start to become significant. The time taken for the scramjet to travel between 63 km and 23 km is approximately 12 seconds, given an assumed constant speed of Mach 10 relative to the local freestream conditions. To model the flight path between 63 km and 23 km altitude, a constant glide slope of  $-75^\circ$  from the horizontal and constant Mach 10 flight was assumed. The time steps used in the calculation are determined by the two-dimensional heat diffusion equation, as discussed later.

## 5.2 Post-Shock Conditions

Before heat fluxes could be determined for each time step, the post-shock conditions were calculated, as these generate the boundary conditions for heat flux to the inlet plates. The high air temperature at the stagnation point and across strong shocks in hypersonic flow implies that the air can no longer be treated as a perfect gas, and the ratio of specific heats will change as temperature rises. Furthermore, at temperatures above 2000 K, oxygen begins to dissociate. To account for the property changes of air at high temperatures, chemical equilibrium was assumed for the calculations. The equilibrium air curve fits used in this analysis were taken from Srinivasan *et al.* (1987). Calculation of the heat post-shock conditions begins with the conservation equations for mass, momentum and energy:

$$\rho_1 u_1 = \rho_2 u_2 \quad (15)$$

$$p_1 + \rho_1 u_1^2 = p_2 + \rho_2 u_2^2 \quad (16)$$

$$h_1 + \frac{u_1^2}{2} = h_2 + \frac{u_2^2}{2} \quad (17)$$

The method described by Anderson (1990) was used to determine conditions downstream of the shock wave using equilibrium air curve fits. The process for both oblique and normal shock regions initially involved guessing a post-shock density value. A corresponding pressure value could be obtained from this using the momentum equation. Post-shock enthalpy was then determined using the equilibrium air curve of Srinivasan *et al.*. An adjusted value for density was then determined using the energy equation. This process was iterated until the density value converged. The post-shock velocity could then be calculated from the continuity equation and the temperature from a curve fit and the known values of density and velocity. A similar iterative process was used for the oblique shock conditions generated in the HyShot flight trajectory. However the deflection of flow due to the ramp angle needed to be considered in this case. The one-dimensional momentum equation was adjusted to account for this. Once the methods were developed, they were coded in MATLAB and the downstream conditions for the normal and oblique shocks were calculated for each time step.

## 5.3 Flat Plate Heat Fluxes

For hypersonic flow, the viscous effects within the boundary layer will cause a temperature profile within the boundary layer at the plate wall (Anderson 1989). A typical cold-wall hypersonic thermal boundary layer profile is presented in Fig. 16, showing the characteristic temperature peak within the boundary layer. At subsonic conditions, flow-to-wall heat flux equations are typically based on the

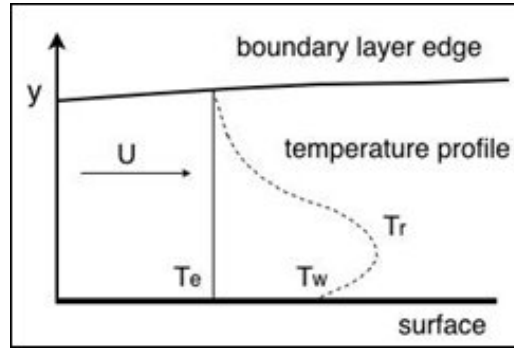


Figure 16: Flat plate temperature profile.

difference between the wall temperature and the air temperature external to the boundary layer. However, due to the temperature gradient within a viscous boundary layer, the heat flux is a relationship between the wall temperature and the maximum temperature within the boundary layer, also known as the recovery temperature. The generalized equations developed by Eckert were used here to determine this reference temperature (Eckert 1955). Considering hypersonic boundary layers, the specific heat of air is likely to change due to the high temperatures. As a result, Eckert proposed that the heat flux to the surface is more accurately predicted using an enthalpy difference rather than a temperature difference between the recovery state and the wall. The equations developed by Eckert for enthalpy difference heat flux, and recovery enthalpy are:

$$q''_w = H_h (h_r - h_w) \quad (18)$$

$$h_r = h_e + r_h (u_e^2/2) \quad (19)$$

where  $h$  (kJ/kg) is enthalpy and  $q''$  (W/m<sup>2</sup>) is heat flux and  $H$  (W/(m<sup>2</sup>K)) is the heat transfer coefficient, evaluated at the reference enthalpy condition. Subscripts  $r$  and  $w$  stand for recovery and wall conditions respectively. In Eqn. 19,  $r$  is the recovery factor and is the square root of the reference Prandtl number, and  $u_e$  (m/s) is the air velocity external to the boundary layer. Equation 19 is derived from the energy equation, Eqn. 17, where the recovery factor  $r$  accounts for the velocity difference between air at the recovery state and the air external to the boundary layer. To calculate the heat transfer coefficient,  $H$ , the relationships for Stanton number and friction coefficient are used:

$$St = \frac{H_h}{\rho^* u_e c_p} = \frac{c_f}{2(Pr^*)^{2/3}} \quad (20)$$

where

$$c_f = \frac{0.644}{(Re_x^*)^{0.5}} \quad (21)$$

Here,  $Pr$  is the Prandtl number,  $c_p$  is the specific heat at constant pressure,  $Re$  is the Reynolds number,  $\rho$  is the air density, and the superscript  $*$  indicates properties obtained at the reference enthalpy condition. Applying this relationship, the heat flux to the flat plate of the first inlet ramp was calculated using

$$q''_{FP} = \frac{0.332 \rho^* u_e (h_r - h_w)}{(Re_x^*)^{1/2} (Pr^*)^{2/3}} \quad (22)$$

where the reference enthalpy values,  $*$ , need to be evaluated at a state which was originally given by Eckert but recently modified by Meador and Smart (2005) to be

$$h^* = 0.45h_e + 0.55h_w + 0.16r \left( \frac{u_e^2}{2} \right) \quad (23)$$



The recovery factor, reference Prandtl number and reference Reynolds number are given by

$$r = \sqrt{Pr} \quad (24)$$

$$Pr^* = \frac{\mu^* c_p^*}{k^*} \quad (25)$$

$$RE_x^* = \frac{\rho^* u_e x}{\mu^*} \quad (26)$$

Where  $\mu$  is dynamic viscosity  $c_p$  is specific heat at constant pressure and  $k$  is the thermal conductivity of the air. Once again, the reference values need to be evaluated at the reference enthalpy condition given by Eq. 23. To calculate air viscosity and thermal conductivity at the reference condition we used the Sutherland power law. In the code, the above process is repeated at each surface node for each time step, resulting in a heat flux distribution around the leading edge and along the top surface for each time step.

## 5.4 Leading Edge Heat Fluxes

Another important aspect of heat transfer at hypersonic speed is the heating of the scramjet leading edge, which influences heat transfer along the plate. We used the analytical method of van Driest, who developed equations for the heat flux to the leading edge of a cylinder, given by (van Driest 1956)

$$q''_{LE} = 0.57 Pr^{-0.6} (\rho_e \mu_e)^{0.5} (h_r - h_w) \sqrt{\frac{du_e}{dx}} \quad (27)$$

The acceleration term in Eq. 27 is the acceleration of the air around the inlet leading edge from the stagnation point to an angle  $\theta$  and is given by

$$\left( \frac{\partial u_e}{\partial x} \right)_\theta = \frac{1}{R} \sqrt{\frac{2(p_e - p_\infty)}{\rho_e}} \quad (28)$$

$$p_e(\theta) = (p_0 - p_\infty) \cos^2 \theta + p_\infty \quad (29)$$

where  $R$  is the leading-edge radius. The pressure and density external to the boundary layer need to be calculated at different locations around the leading edge from the stagnation point using a Newtonian pressure distribution:

$$p_e(\theta) = (p_0 - p_\infty) \cos^2 \theta + p_\infty \quad (30)$$

where the subscript  $_0$  indicates the location of the stagnation point. At a given location downstream of the leading edge, the enthalpy was calculated using the energy equation 17, and the density determined using equilibrium air enthalpy curve fits (Srinivasan et al. 1987). Once the acceleration term was determined, the heat flux at different locations around the leading edge could be calculated, as shown in Fig. 17. Due to the finite-element mesh not modeling the curvature of the leading edge and only employing one-dimensional boundary conditions, it was necessary to sum the heat flux over the leading edge surface and distribute the total leading edge heat flux among the leading edge mesh nodes. The leading edge heat flux is the area under the red flux distribution in Fig. 17, and is represented in the code by the blue flux distribution, which has the same total heat flux as for the red curve. A quarter-elliptical distribution was used to achieve the redistribution to the mesh nodes.

Another important adjustment made in the heat flux calculations was for the heat flux at the maximum  $\theta$  and  $x = 0$  of the flat plate to be matched (Odam et al. 2005). Considering the flat plate heat flux, Eq. 22, if  $x = 0$  an infinite heat flux is produced due to the Reynolds number term in the denominator. Therefore an offset for  $x$  needs to be added to account for the boundary layer thickness at this location. In the analysis, the  $x$  offset was calculated by equating the leading edge and flat plate heat flux for the point between the curved leading edge and flat plate.

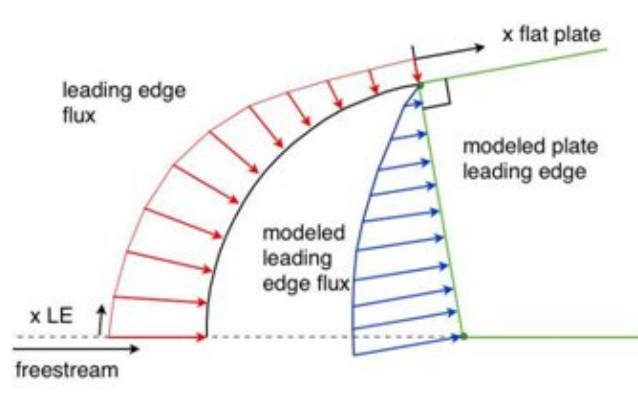


Figure 17: Assumed leading edge heat flux distribution.

## 5.5 Two-Dimensional Heat Diffusion

Once the heat fluxes were calculated, the remainder of the problem involves modeling the transfer of heat through the plate using the finite-element method. An initial saturated plate temperature of 300 K was chosen for the start of the analysis. In order to account for the heat transfer through the modeled plate, the two-dimensional heat diffusion equation was used:

$$\frac{\partial^2 T}{\partial x^2} + \frac{\partial^2 T}{\partial y^2} = \frac{\rho C_p}{k} \frac{\partial T}{\partial t} \quad (31)$$

where the density, specific heat and thermal conductivity are that of the plate material. The  $x$  and  $y$  components are the two spatial dimensions of the plate, and  $t$  denotes time. The above heat diffusion equation has been derived from the energy equation using a second-order Taylor-series expansion. Equation 15 was then discretized using a forward-time-central-space (FTCS) scheme to give the following difference equation (Anderson 1995):

$$T_{i,j}^{n+1} = T_{i,j}^n + \frac{k\Delta t}{\rho c_p} \left[ \frac{T_{i+1,j} - 2T_{i,j} + T_{i-1,j}}{\Delta x^2} \right]^n + \frac{k\Delta t}{\rho c_p} \left[ \frac{T_{i,j+1} - 2T_{i,j} + T_{i,j-1}}{\Delta y^2} \right]^n \quad (32)$$

where  $i$  represents the node number in the  $x$  direction,  $j$  represents the node number in the  $y$  direction and  $n$  represents the time step index. The difference equation sets a template, which allows the heat diffusion equation to be applied to the finite-element mesh. Fourier's law was used to transfer the heat calculated for each node to the finite-element nodes. This allowed the flux boundary conditions to be enforced as a temperature gradient between the surface node and the node directly below the surface. To enforce this boundary condition, the use of ghosting points around the finite element mesh was necessary. The following criterion determining time step size was used to ensure solution stability (Anderson 1995):

$$\frac{k\Delta t}{c_p \rho \Delta x^2} \leq 0.5 \quad (33)$$

## 5.6 Computation Results

The time steps for the modeled flight depended on the material used. For aluminium, approximately 35000 time steps across the 12-second flight time were required, with approximately 9000 time steps required for steel. The final code took approximately 2 hours for a steel model and approximately 6 hours for an aluminium model on a 3 GHz Pentium 4 personal computer running MATLAB R2007b. Typical outputs extracted from the code include time-varying and spatially varying temperature and heat flux values at specified nodes. Another important output of the code is a comparison of the energy transferred to the plate via convection to the internal energy rise of the material. This output



Parameter	Standard calculation $dt = 1.4 \times 10^{-3}$ s $dx = 1$ mm	Reduced time steps $dt = 7 \times 10^{-4}$ s $dx = 1$ mm	Reduced spatial steps $dt = 1.4 \times 10^{-3}$ s $dx = 0.5$ mm
Plate base $T$	332.02 K	332.00 K	332.02 K
Leading-edge $T$	1644.0 K	1643.8 K	1651.5 K
Internal energy	$1.7751 \times 10^6$ J	$1.7742 \times 10^6$ J	$1.7749 \times 10^6$ J
Convective energy	$1.7477 \times 10^6$ J	$1.7468 \times 10^6$ J	$1.7468 \times 10^6$ J

Table 1: Effect of step size on heat flux calculation

gives an indication of whether the code obeys the conservation of energy. The differences between these energy values are typically below 3.5 % for aluminium and 1.6 % for the steel plate, mostly due to averaging equations used in the calculation of the two energy values.

In order to quantify the effects of changing node spacing and time step size on the output of the code, a sensitivity analysis was conducted. The outputs compared were temperature at the base of the plate after 12 seconds, leading edge temperature after 12 seconds, and energy calculation values. The results of halving the time step and the grid size individually are compared to the standard code in Table 1 for the same conditions, though using a larger plate angle than the  $5^\circ$  half-angle used for the other results in the paper.

It is clear that the effects of halving both the time step and the grid size are small. The greatest percentage difference is less than 0.5 percent, due to the leading edge temperature after 12 seconds.

It was also possible to decrease the calculation time by assuming constant reference Prandtl number rather than iteratively calculating a value at every step using Eq. 25. When incorporating a variable Prandtl number in the MATLAB code, the steel plate calculation took over 10 hours and the aluminium plate calculation over 25 hours to complete. To justify the assumption of constant reference Prandtl number, a comparison of the two methods was conducted. The range of computed Prandtl numbers over the duration of the flight is small — between 0.69 and 0.715, compared with the assumed constant  $Pr = 0.7$ . For the evaluation point temperature on the underside of the plate, the difference between the two methods was less than 0.05 percent. For the leading edge temperature, the difference was approximately 2 percent. For total energy, the difference was approximately 1.4 percent. Since the effect of varying  $Pr$  at the evaluation point is negligible, a constant  $Pr$  was considered a reasonable assumption for the calculations.

## 5.7 Typical Results

As mentioned above, the results presented here are based on a generic two-dimensional flat plate inlet operating at a constant Mach 10 and at zero angle of attack, with each plate angled at 5 degrees to the freestream. The flight profile used was similar to that shown in Fig. 3, with an angle to the horizontal of 75 degrees. The primary output for the analysis is a temperature vs. time plot of the node 400 mm from the leading edge, on the underside of the plate. This point was chosen because it is a reasonable estimate for the location of the optical system's window, as illustrated in Fig. 15. The temperature histories for 10-mm-thick aluminium and steel plates are shown in Fig. 18. The temperature at the selected node rises exponentially over the 12-second test time in both cases. This is due to the transfer of heat from the surface through the plate and the increasing surface heat flux as altitude decreases and the density of the external flow increases. The aluminium has a higher temperature than the steel at the selected node after 12 seconds, due to the higher thermal conductivity of aluminium. It should be noted, however, that in a real application it is unlikely that inlet walls made from the two materials would be the same thickness. The higher density and strength of steel would ensure that a thinner sheet would be used for that material than for aluminium.

In this calculation, the aluminium has a maximum temperature of 319.5 K and the steel has a

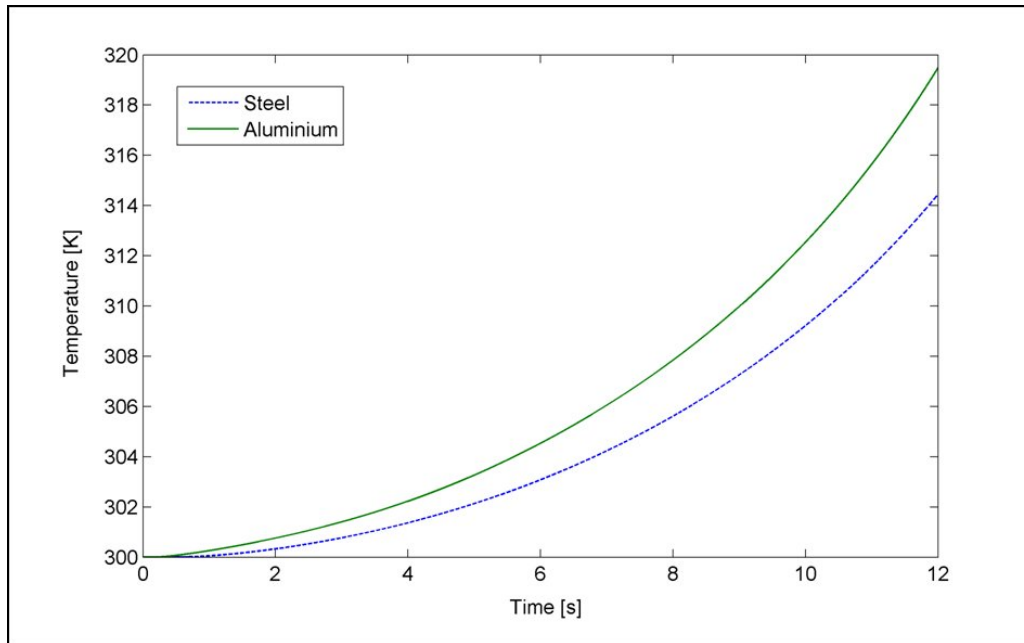


Figure 18: Surface temperature history for two metals.

maximum of 314.5 K, while the upper operating temperature limit for the optics is 333 K. Taking into consideration the heat transfer through the components box, the temperature within the box will not exceed the 333 K upper temperature limit at these conditions. Based upon these results, the laser optics system would continue to operate at these conditions down to the 23-km lower-height limit. However, any increase in angle of attack would further raise the temperature of the plate, and might exceed the required maximum temperature for the optics. This illustrates the need for modeling of the inlet heat loading for flight experiments containing temperature-sensitive equipment.

Spatial temperature gradients can be used in experiments to test the survivability of components such as the optical system's fused silica windows or to determine a safe distance downstream of the leading edge where the components can be located. Figure 19 is a plot of the temperature profiles within the modeled steel plate. The y-axis has been expanded to clearly show the contours. The temperature at the surface near the window is approximately 330 K, and the temperature at the bottom of the plate near the window is approximately 310 K. It is apparent from Fig. 19 that most of the heat transfer to the plate occurs very close to the leading edge, and the majority of the plate remains at or near the pre-test soak temperature.

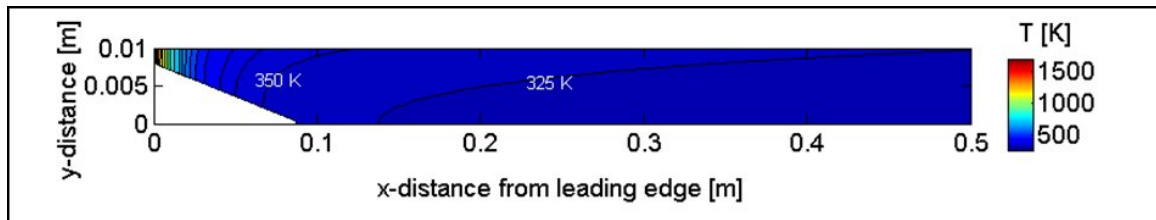


Figure 19: Two-dimensional temperature contours for steel model at  $t = 12$  s.

## 5.8 Comparison with Previous Work

Our computation has been compared with previous work by Odam et al. (2005) at conditions as close as possible to the conditions used in that study, to show that this calculation produces comparable heating results. A comparison of the code with a standard CFD package would require such a

package to be closely coupled to a finite-element heat transfer code, as the boundary conditions for both the fluid and heat transfer problems are continuously varying during the flight. As we do not have such a code, we have compared against Odam *et al.*, which was shown to compare well with computations performed at discrete points along the trajectory and is the closest code with similar functionality known to the authors. The two computations were not identical, as Odam *et al.* matches the stagnation-point heat flux to the flat plate heat flux in a slightly different manner to this study, and models the heat capacity variations with temperature, while this calculation assumes a constant heat capacity for a given material. The heat transfer through the plate was calculated by Odam *et al.* using a commercial finite-element code rather than the custom code used in the present work. In addition, the Mach number in that study varied from 9.6 to 10.3 during the descent, but was fixed at Mach 10.0 throughout the descent in our code.

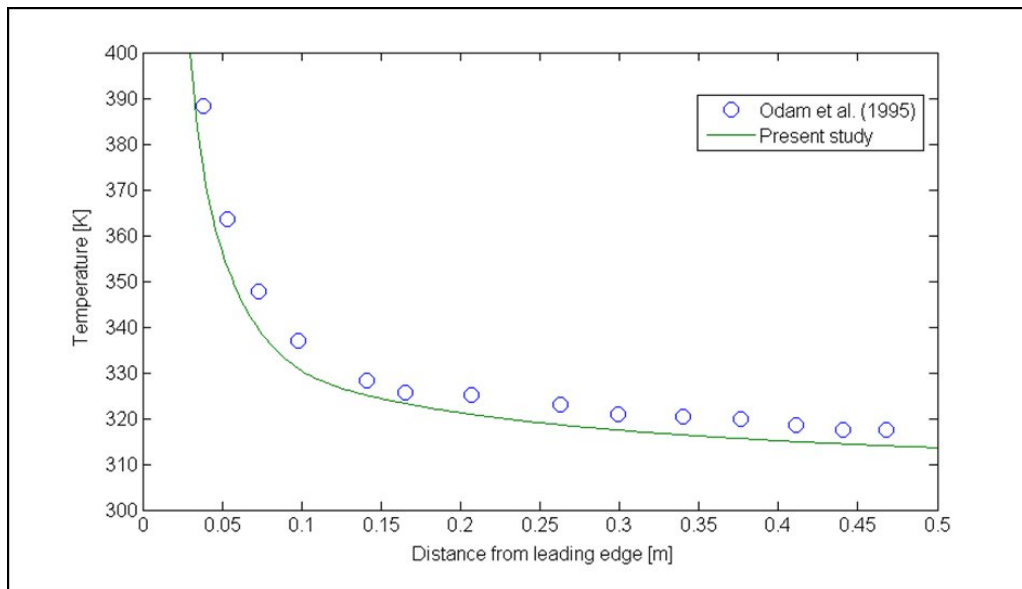


Figure 20: Comparison of final temperature at the top of the plate at 30 km altitude with the calculations of Odam *et al.* (1995)

The wetted plate surface temperature for Odam *et al.*'s trajectory at zero angle of attack is directly compared with our equivalent calculation for a 4.3-degree half-angle inlet in Fig. 20. The codes were both run assuming an initial temperature of 300 K at 63 km altitude and a final altitude of 30 km. The two temperature distributions at this time disagree somewhat at the leading edge, but the difference in the downstream part of the plate, where the optics would be located, is approximately 5 K.

## 5.9 Limitations of Heat Flux Analysis

As the code was designed to be a simple tool for predicting heat transfer in two-dimensional scramjet inlet flows, there are some limitations to its applicability. First, the heat flux calculations deal with convective fluxes only, and do not consider radiative heat flux. At the flight conditions along the inlet surface, convective heat transfer should dominate radiative heat transfer. At the stagnation point, where the air to material temperature differ most, radiative heating may be significant.

Another assumption made was that the analysis started at 63 km altitude on the descent, with a saturated plate temperature of 300 K. This saturation temperature is an engineering estimation presented in previous heat transfer analyses (Odam *et al.* 2005). The choice of initial saturation temperature will influence the results. Therefore, it needs to be accurately predicted for each flight profile based either upon measurements or more comprehensive calculations. It may be possible to extend the heat transfer analysis to cover the whole mission profile if the air properties can be determined for high

altitudes. Doing this will also allow the cooling aspects of high altitude flight to be investigated to determine TDLAS survivability.

With respect to the adiabatic boundaries, the assumption is that no heat is transferred through these surfaces. For the wedge section of the leading edge shown in Fig. 15, the adiabatic condition only applies if the scramjet leading edge is symmetric to the freestream axis, as the modeled plate then forms one half of a two-sided inlet. If the leading edge is not symmetric, then there will be uneven heat flux distributions on either side of the leading edge, resulting in heat transfer across the wedge boundary. The lower plate in the inlet cowl would also need to be added to the model to take this effect into account, which is a relatively simple addition to the code.

One final study that will be undertaken with the code in future involves determining the effect of angle of attack on the heating, as the inlet can be angled by  $\pm 6^\circ$  during flight, and this can have a significant effect on the heating of the inlet plates. The current calculations, performed for zero angle of attack, show that the peak temperature during flight is of the same order as the maximum temperature that can be tolerated by the optical system. At high angles of attack this heat loading will be higher, and this needs to be accounted for in our designs. We are currently investigating the effect of placing refractory insulating materials between the optical assembly and the inlet plates to further reduce the heat transfer at these higher attack angles.

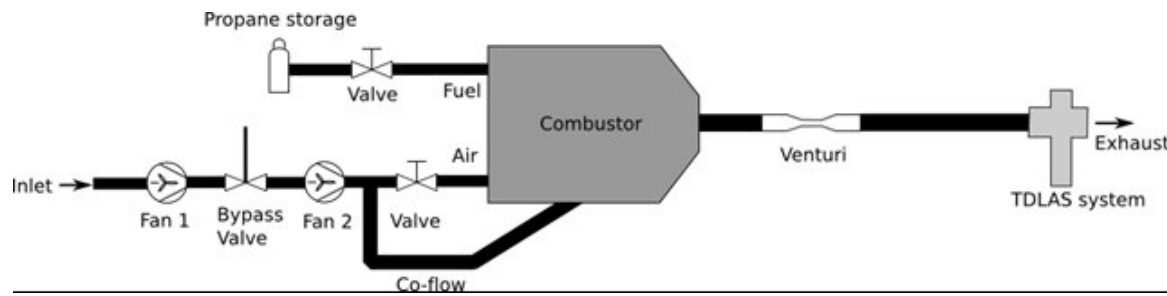
## 6 High-Temperature-Operation Tests

This section describes work published in O’Byrne et al. (2009) on the performance of a TDLAS sensor based upon a VCSEL at high temperature. Unlike the rest of this report, the work was performed on water vapor absorption at 940 nm rather than oxygen absorption at 760 nm because the experiments were performed at the exit of a combustor. Despite this point of difference, the laser system components and the type of laser were the same as those used in the inlet tests. The water vapor absorption tests were performed at temperatures comparable to those that would be experienced at the plate surface during a hypersonic flight test, according to Sec. 5.

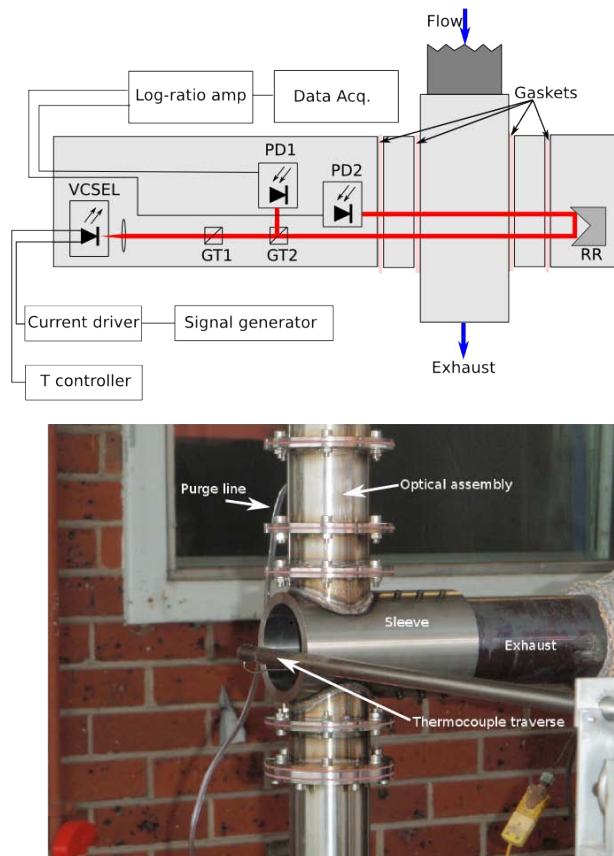
The experiments were performed at the Infrared Suppressor Test Facility at DSTO Fishermans Bend. The main components of the facility, an LPG-fired air heater, are shown in Fig. 21(a). It consists of a combustor burning propane in air, supplied to the combustor by a pair of fans. Valves control the ratio of air to propane fuel entering the annular combustor, and the system introduces a co-flow of cooling air that mixes with the combustion products at the combustor exit. A venturi placed in the pipe downstream of the combustor allows for measurement of mass flux at the combustor exit, followed by a 76-mm outlet tube that exhausts into the atmosphere. A traversing thermocouple is placed at the exit of the facility with another thermocouple located near the venturi. These, along with the valves controlling supply of fuel and air, are used to provide an exhaust temperature of between 293, 453, 753 and 873 K. The system has no other way of quantifying the composition of the gas, and there is no measurement of fuel mass flow. For this reason, a sensor capable of nonintrusively measuring the temperature and water vapor concentration of the exhaust gas was considered desirable.

The diode laser system was implemented within a stainless steel arrangement that mounted directly to the exhaust pipe of the facility, as shown by the cruciform shaded region in Fig. 1. The optical design of the system is shown in Fig. 21(b). The system consists of a ULM Photonics ULM948-01-TN-S46FT temperature-controlled VCSEL, controlled by a Newport 325B temperature controller and a Newport 501B current controller. A ramp signal from a signal generator was used to provide the current modulation signal that varied the wavelength.

The system is very similar to that described in Fig. 23, except that components are mounted in a Thorlabs 30-mm cage system, for ease of setup. Each of the rods was hard-mounted to the 316 stainless steel casing to make the mounting as rigid as possible. A thermally isolating section of casing is mounted on each side of the exhaust sleeve, connected to the optical assembly casing by four



(a) Exhaust simulation apparatus



(b) Optical apparatus

Figure 21: High-temperature test system

paper gaskets. Both sides of the assembly are purged by a flow of dry nitrogen at 1 liter per minute. This purge prevents water vapor from the exhaust entering the assembly and provides cooling for the optics. Nitrogen is allowed to flow out of the holes in the sleeve. The nitrogen flow rate is very low compared to that of the exhaust gas, and has minimal effect on the exhaust flow. The combination of the gaskets and purge kept the optical system cool, and the optics mounts did not exceed 10 K above ambient even for the highest exhaust gas temperature of 873 K.

Light from the laser passes through a collimator and two Glan-Taylor prisms, labeled GT1 and GT2 in the diagram. The first prism allows only one polarization component of the laser to propagate through the system, while the second prism splits the beam into two beams of equal intensity. One of the beams is directed onto PD1 and acts as a reference signal, while the other beam passes through two 12-mm-diameter apertures in the sleeve to a retroreflector, where it is redirected for a second pass through the exhaust flow and onto a log-ratio amplifier circuit that amplifies the absorbance directly. The amplifier circuit also contains a linear pre-amplifier that amplifies the output by 82 times to fill the dynamic range of the National Instruments PCI6115E digitizer card. The 45-kHz bandwidth of the



log-ratio amplifier provides an upper measurement limit of 150 spectra per second. A retroreflector was used at the opposite end of the exhaust to provide two passes through the flow, with a total path length of 152 mm.

Figure 21(b) also contains a photograph showing the apparatus attached to the exhaust of the IRSTF, with the traversing thermocouple used to measure temperature across the exhaust for comparison with fitted TDLAS temperature values.

## 6.1 High-Temperature Test Results

Thermocouple temperature measurements were performed during the facility run at the exit temperatures of 453, 753 and 873 K. Two things are clear from these distributions: the peak temperature is spatially uniform when averaged over the sampling time of the thermocouple, and the width of the flat peak temperature region decreases as the temperature increases. This causes difficulties for the path-averaged TDLAS measurements. A single temperature fit will be biased towards the cold part of the flow, underestimating the peak temperature.

To account for this colder gas, the exhaust flow was modeled as a top-hat distribution containing two components: an outer sheath of known length at the conditions measured using the fitted spectra with fans on but no combustion, and an inner core of hot gas whose temperature and mole fraction could be fitted. A sample result from fitting this compound spectrum is provided in Fig. 22. The measured cold gas temperature was 354 K and water mole fraction of 0.041. Fitting the data in this way for the nominally 754 K exit temperature produced a peak temperature of 735 K and a water mole fraction of 0.09. This is quite a reasonable fit, although the larger peak was not fit as well as the compound peak. The nominally 873 K temperature fit produced in the same manner generated a peak temperature of 821 K.

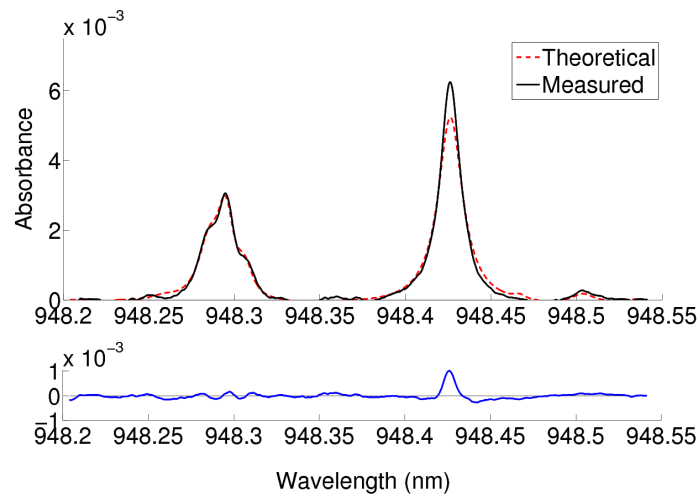


Figure 22: Fit for water vapor spectrum at 735 K and H<sub>2</sub>O mole fraction of 0.09

More importantly to the current investigations is the fact that these experiments were performed at a flow temperature of up to 873 K. The facility was run for up to 10 minutes at a time, with data recorded over the entire run time. The combined effects of the nitrogen purge and the gasket material separating the sections of the detector tube shown in Fig. 21(b) prevented the system from getting hotter than 10 K above room temperature even for the hottest sustained exhaust product flow. As the system has been tested in an oven and shown to perform at temperatures up to 40 K above ambient (Long 2008), the system should be able to survive under flight conditions at an altitude of 30 000 m in Mach 10 flight for a similar duration. As the duration of a flight test is around 6 seconds, a system similarly insulated and purged should be able to comfortably operate without encountering overheating problems.

$p_0$	$T_0$	$p_\infty$	$T_\infty$	$u_\infty$	$p_{pitot}$
MPa	K	Pa	K	m/s	kPa
$0.8 \pm 0.08$	550	600	68	900	30

Table 2: Freestream flow parameters for hypersonic tests.

## 7 Hypersonic Facility Tests

The hypersonic inlet tests were performed in the University of Southern Queensland’s free-piston-driven Ludwig tube facility (Buttsworth and Smart 2010). This facility has a number of properties that make it well suited to the development of the diode laser oxygen sensor. As it is a very new facility, the flow has not been adequately characterized, which means that this method can provide useful time-resolved data about the inlet freestream conditions. Also, because the facility operates at lower enthalpies than shock tunnels, the duration of the flow is considerably shorter. In the USQ tunnel, the flow duration is 0.2 seconds, some 200 times longer than the test time of the T-ADFA facility. Because the laser scan rate is limited to 200 Hz or less by the 50 kHz bandwidth of the log102 log-ratio detector, the duration of flow in the Ludwig tube allows some 15–20 scans to be obtained during a run, which provides valuable time history data for the flow. Finally, because the freestream temperature is approximately 60 K, the transition strengths are high, and the signal-to-noise ratio of the absorption signal is significantly higher than it would be in a higher-enthalpy facility.

The tunnel consists of a 16-m-long Ludwig tube connected to a Mach 6 hypersonic nozzle. A high-pressure air reservoir providing an initial pressure of about 20 MPa drives the piston down the tube, compressing the air in front of the piston until the single diaphragm located at the nozzle entrance ruptures and allows the gas to flow through the nozzle into the test section. The flow conditions generated at the nozzle reservoir and nozzle exit are summarized in Table 2.

The uncertainty in stagnation pressure is due to the variability in the measured stagnation pressure, as there are several high-frequency fluctuations in the pressure in the nozzle reservoir, which was measured using a piezoelectric pressure transducer. These fluctuations are due to the complex system of compression and expansion waves traveling along the Ludwig tube and the nozzle. During the 0.2-second test time, the average nozzle reservoir pressure increased from 830 kPa to 890 kPa. Although the inviscid Mach number of the nozzle is 6.0, the displacement thickness of the boundary layer reduces the Mach number to approximately 5.8. Propagating the uncertainty in stagnation pressure, temperature and Mach number produces an uncertainty in the nozzle exit conditions in Table 2 of approximately 15 %.

### 7.1 Arrangement for Hypersonic Experiments

The basic arrangement of the system is similar to that of the previously described experiments, with the same electronic system used to generate the variable current ramp, control the diode laser and provide the log-ratio amplification. Figure 23 shows a cut-away drawing of the optomechanical system. As for previous experiments, the signal was amplified using a circuit based upon the Texas Instruments log102AID monolithic log-ratio amplifier chip. The arrangement for the hypersonics experiment went through a period of refinement to simplify the layout, minimize the size of the system and facilitate the adjustment of the system. In addition, unlike the experiments described previously, the experiments are performed at a freestream pressure 600 Pa. This means that the absorbance over the roughly 250-mm distance of a single pass was of the order of  $10^{-5}$ – $10^{-4}$ . Such low absorbances are very difficult to measure, even using a log-ratio detector. Because of the limitation on the size of the absorption region, it was necessary to increase the number of passes through the inlet, and this was done using a pair of matched retroreflectors, mounted on either side of the inlet. Use of retroreflectors rather than mirrors ensures that the laser traverses across the inlet are all parallel.

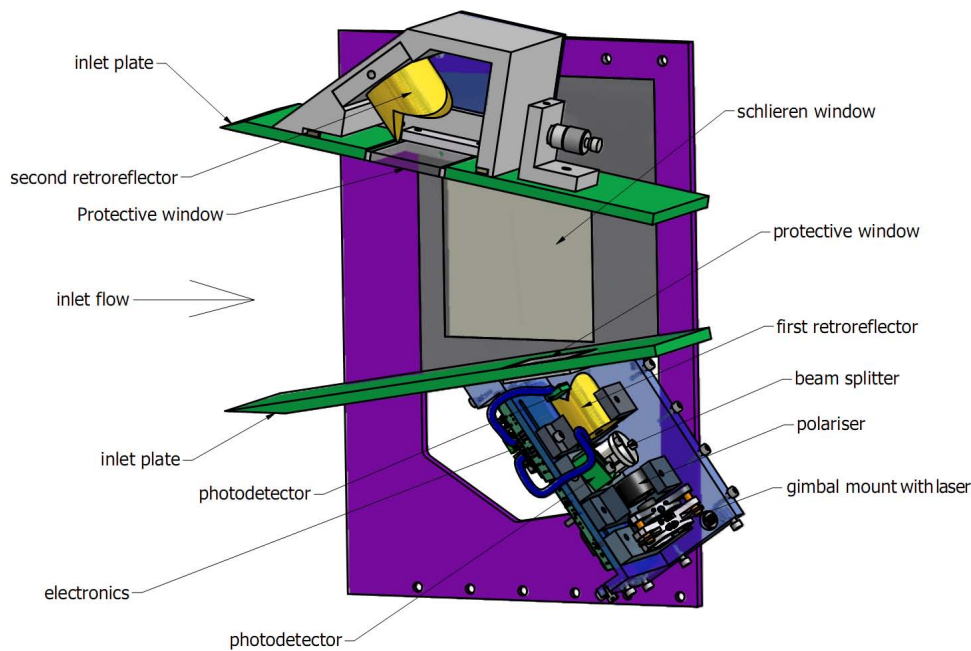


Figure 23: Schematic of TDLAS optics for hypersonic inlet measurements.

The experiments were performed in two configurations. The first used the inlet configuration shown in Fig. 23, with the laser passing 4 times through the freestream and the two shock layers. The second configuration removed the plates from the flow altogether and passed the laser four times through the entire nozzle flow. The retroreflector was mounted from the top of the tunnel. In the second configuration, the effect of the shock layers is minimized and the path length through the flow is maximized. Because the nozzle flow hits the mount for the retroreflector, the retroreflector was protected by an aluminium shield that penetrated into the nozzle flow, without significantly disturbing the flow itself, and removing the effect of the nozzle boundary layer. The beam did, however, pass through the nozzle boundary layer on the lower side because space restrictions did not allow a second shield to be installed in the system. The two arrangements are shown schematically in Fig. 24. The optical and electronic setup of the experiment was identical for both arrangements. The idea behind testing in these two ways was to determine the effect of the shock layers on the ability to determine the freestream velocity. The arrangement that passed through the entire nozzle flow also increased the total path length through the flow considerably, possibly increasing the signal-to-noise ratio of the experiments.

The nozzle configuration was achieved by taking the lower plate of the inlet configuration and mounting it below the nozzle outside of the flow field, using a pair of steel brackets suspended from the plate mounted above the nozzle, as shown in Fig. 24. The upper plate and window were not used: a separate mount, again suspended from the upper plate, held the retroreflector and protective channel.

## 7.2 Data analysis

The spectra produced using the four-pass inlet configuration is shown in Fig. 25. Figure 25(a) shows all the spectra from one of the tunnel runs, plotted as a function of time. Each spectrum contained 5000 data points, to properly sample the absorption lines. In this plot there is an obvious change in the baseline level of the spectrum, caused by shaking of the optical system as the tunnel recoils. This drop in signal was removed once the system was better stabilized. The regularly spaced spikes in the plot indicate the start of each spectrum. It is also apparent that the overall level of noise is significantly higher during the tunnel run than either before or after the run. This is due to a combination of vibration and flow noise within the facility.



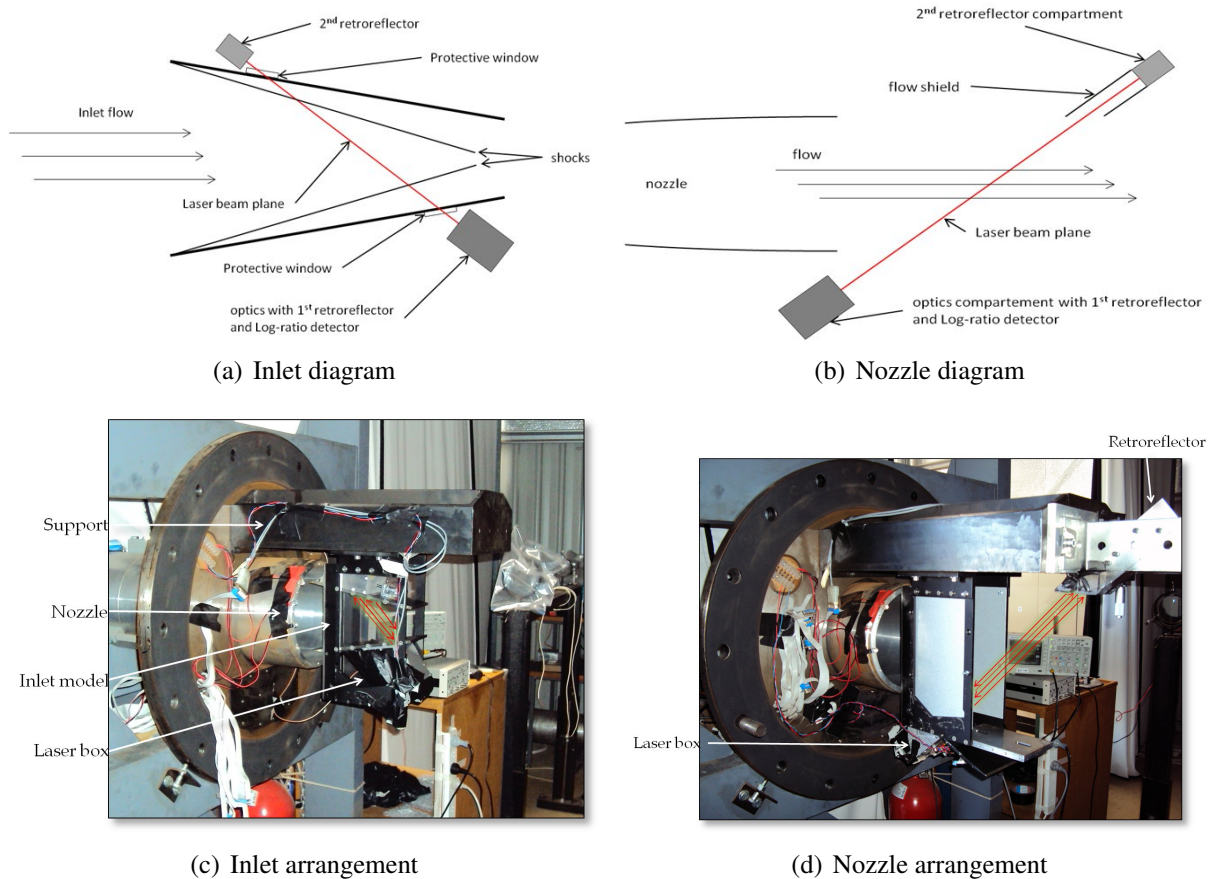


Figure 24: Two arrangements for hypersonic facility measurements.

Figure 25(b) shows one of the spectra in Fig. 25(a), with the log ratio signal plotted as a function of wavelength. The blue trace is the measured spectrum during the flow time, while the red trace is the spectrum in the test section immediately before the tunnel operates. The red spectrum shows the absorption features at zero velocity. There are four such lines in the scan around 760.5 nm. The blue spectrum has a number of spikes, most of which arise from vibration noise. By comparing the absorption lines in the red spectrum with the blue spectrum, it becomes apparent which of the spikes correspond to absorption lines. In each of these cases, the blue spectrum shows two lines that are equidistant from the center of the red absorption line location. The two lines occur because the absorption lines are Doppler shifted depending on the direction of beam propagation, as described in Section 3. The lines in the tunnel flow are thinner than those in the quiescent tunnel gas because the tunnel flow is much colder: 60 K compared with 300 K. Figure 25(c) focusses on a single absorption feature in the scan, showing more clearly the difference between the quiescent absorption feature and that in the inlet flow.

Figures 25(b) and (c) also show that the absorption signal contains significantly more noise during the tunnel run than before or after it, again most likely due to a combination of flow noise and vibration. Despite there being peaks throughout the spectrum in Fig. 25(b), the only places where the peaks are doubled are at the locations of the peaks in the red spectrum. This allows us to differentiate between the noise peaks and the absorption signal.

As each spectrum contains four absorption lines, each of which is Doppler-shifted by the same amount, each scan has four independent measurements of velocity. As explained in Sec. 3, the velocity measurement is insensitive to fluctuations in the amplitude of the signal, and so even in the presence of a significant modulation in the baseline signal, the velocity can be accurately measured for each of the absorption lines. This is done by fitting the absorption signal with two Gaussian peaks, as shown in Fig. 26.

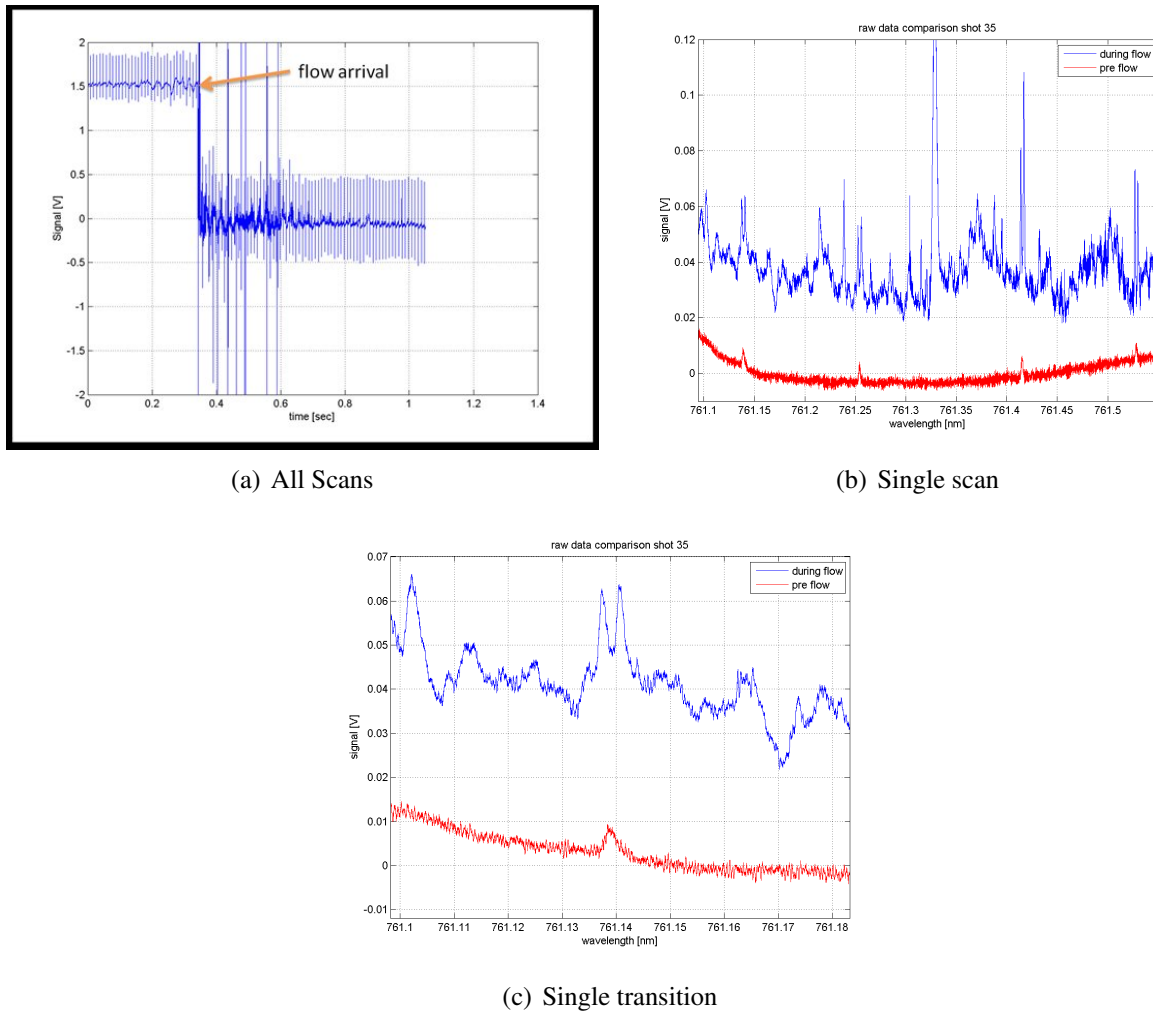


Figure 25: Inlet absorption spectra

Figure 26 shows both the data and the fit, with the residual plotted beneath them both. The fit is achieved by using a Levenberg-Marquardt nonlinear least-squares routine to fit the amplitude, width and location of the two Gaussians to each of the spectra. This was done separately for each of the pairs within each spectrum, to reduce the effect of changes in the background across a scan. Although in theory the two Doppler-shifted peaks should have the same width and amplitude, changes in the background can make the amplitude of the peaks look different, which is why the amplitudes of the two absorption features are computed independently. Because each spectrum contains four lines, each spectrum has four independent velocity measurements, increasing the measurement rate to 600 measurements per second for a 150-Hz scan rate.

It was not possible to measure a velocity for every absorption feature, particularly for those parts of the spectra where spurious peaks interfere with the velocity measurements. Any data with more than two peaks in the vicinity of the known absorption feature was not used for a velocity measurement. Considering all of the spectra obtained during the test time, the measurements had a standard deviation of 70 m/s. If all four absorption lines are used to obtain a single velocity measurement, the standard error drops to  $\pm 40$  m/s.

Figure 27 shows the measured velocity for each of the four lines over the 0.2-second history of the flow for a single tunnel run. The velocities using each of the four transitions are shown in different colors. It is clear from the plot that there is no particular relationship between the absorption line used for the velocity measurement and the velocity measured using that transition. In this case the standard deviation is around  $\pm 40$  m/s between extremes of 800 and 1050 m/s. It is clear from Fig. 27 that a very

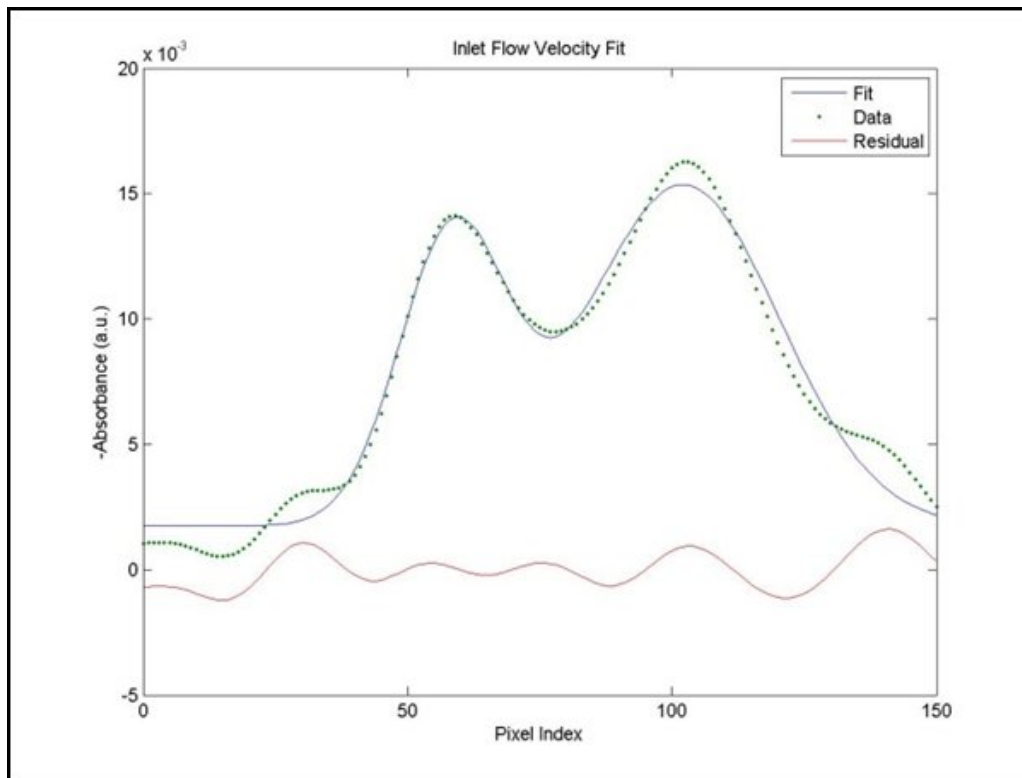


Figure 26: Least-squares fit to the Doppler-shifted absorption feature.

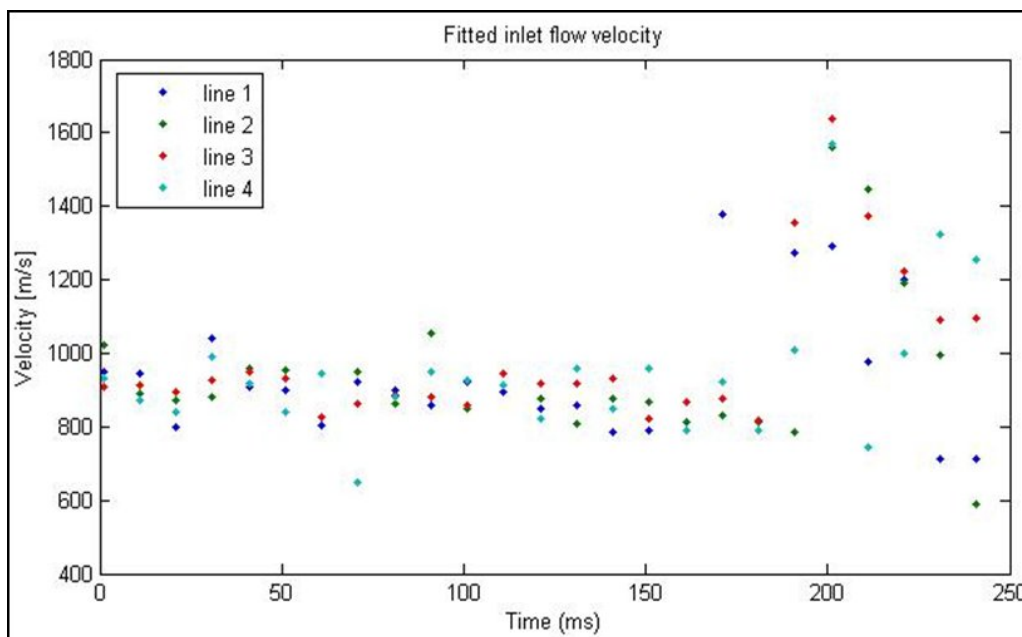


Figure 27: Velocity as a function of time throughout the nozzle flow time, inlet configuration.

sudden change in behavior occurs at 180 ms after the onset of flow. This corresponds to the end of the test time and the onset of unsteady nozzle flow in the facility. The much larger spread of velocity data makes it apparent that the flow behavior is fundamentally different to the uniform flow speed generated during the test time. Figure 27 also clearly shows a downward trend in the velocity during the test time. This decrease in velocity is caused by the combined effects of reduced nozzle reservoir pressure and temperature as the run progresses. Both of these effects cause the nozzle boundary layer displacement thickness to increase over the test time, reducing the effective nozzle Mach number.

The velocity measurements were repeated for three tunnel runs. These three runs produced ve-

locity measurements that did not vary outside the standard deviation for one run from one run to the next. Considering the data from all three runs, the freestream velocity at the beginning of the run was  $912 \pm 40$  m/s. Averaging all the velocity measurements between  $t = 0$  and  $t = 180$  ms produces a mean velocity of 900 m/s. This is consistent with the calculated 900 m/s in Table 2, although given the uncertainty in both the measurement and calculation, the closeness of these results should be considered coincidental. The consistency in the velocity measurements can be explained by the simplicity and consistency of the Doppler-based measurement technique.

As mentioned previously, in addition to the inlet measurements velocity was also measured using the entire nozzle flow, to maximize the absorption signal, because over four passes through the system the beam passed through nearly 4 m of the nozzle flow, with no shock layer flow included. Interestingly, however, there was no significant difference in the signal-to-noise ratio of the measurements compared with the 1-m path length inlet measurements. This implies that although the signal increases due to the additional absorption, the noise from the flow and from the vibration of the system increases commensurately. One problem with this configuration was that the lower inlet plate was attached to a drilled plate above the nozzle. This cantilevered arrangement was susceptible to vibration, even when braced, and this increases the vibration noise. With the four times longer path length of the nozzle configuration, the same angular displacement of the beam will cause a four-times greater spatial displacement of the beam on the detector surface, leading to a noisier absorption signal if this displacement is great enough for the beam to partially miss the  $10 \text{ mm} \times 10 \text{ mm}$  photodiode surface.

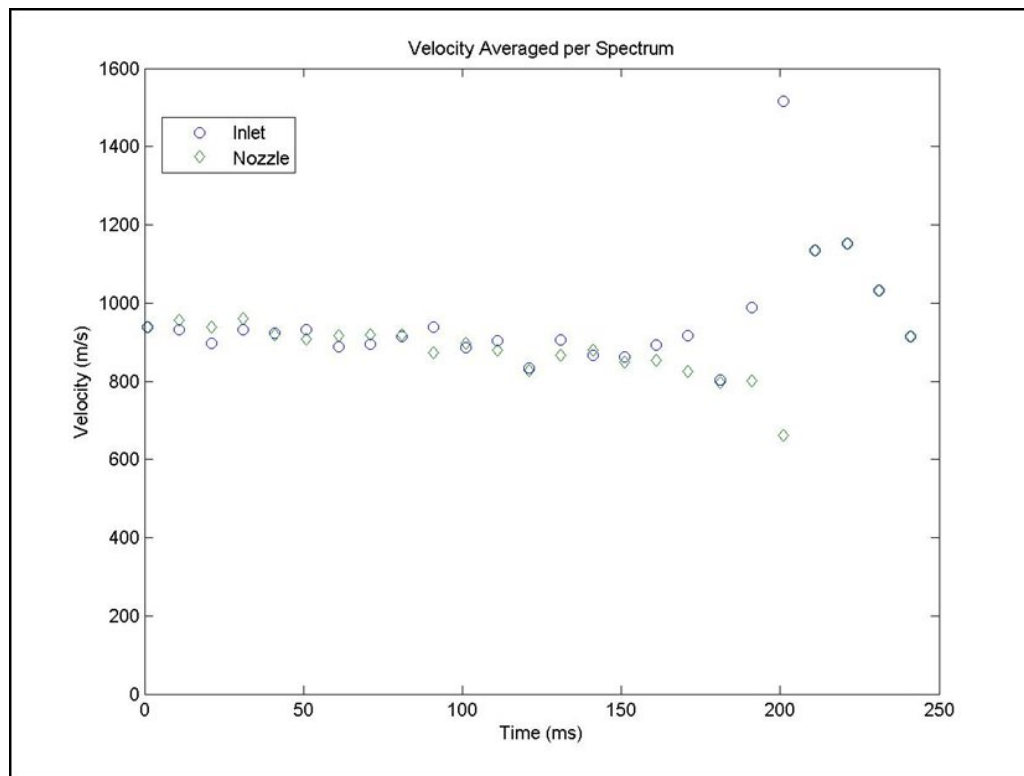


Figure 28: Comparison of velocities measured using inlet and nozzle configurations.

Figure 28 compares the averaged velocities measured over three runs at each of the two configurations. As the plots show, the velocities are consistent between the two configurations. This fact carries two implications: first, the shock layers in the inlet configuration have very little effect on the measured freestream velocity, because the absorption in the freestream dominates the absorption in the shock layer, and secondly the variability in the two configurations is nearly the same. The similar variability in the two signals is due to the insensitivity of the velocity measurement to amplitude noise in the signal. Both measurements show a large increase in scatter at 180–200 ms after flow initiation,

which was also consistent with high-speed schlieren measurements taken at the same flow condition, and both measurements indicate the same downward trend in velocity of approximately  $110 \text{ m/s}^2$ . The agreement between the two measurements is particularly notable because the angle of the laser to the flow is different for the two configurations.

The amplitude noise apparent in Fig. 25 and the analysis in Sec. 3 indicate that the system is not sensitive enough to measure the angle of attack of the vehicle in either the current inlet or nozzle configurations. For this reason, all measurements were performed at zero angle of attack. Unless the absorption signal has sufficiently low noise to measure the absorption in the shock layers, there will not be sufficient sensitivity to angle of attack to make a sufficiently accurate measurement.

### 7.3 Temperature Measurements

Unlike the velocity measurement described in the preceding discussion, which depends only on the frequency shift of the absorption line, temperature is measured as a ratio of absorption signals. This fact makes the temperature measurement much more susceptible to amplitude noise in the absorption signal. Although the temperature measurement has significantly greater noise than the velocity measurement for this reason, the sensitivity of the absorption signal to temperature at these very low temperatures is high, and helps to compensate for the noise.

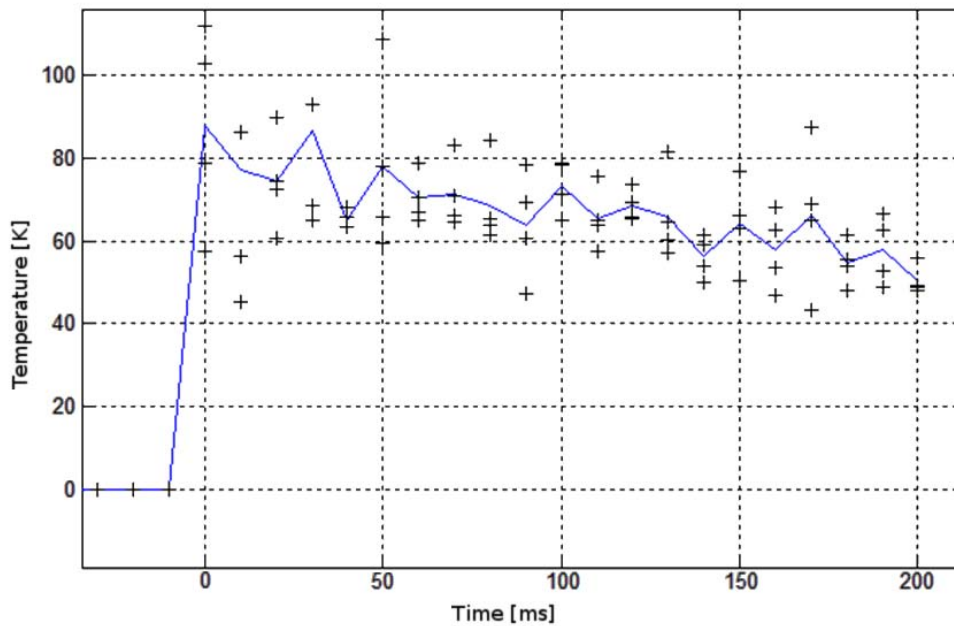


Figure 29: Temperature as a function of time throughout the nozzle flow time, inlet configuration.

The averaged time history over four tunnel runs is shown in Fig. 29. As the plot shows, there is significant scatter in the temperature data over the run time. The standard deviation in temperature is approximately  $\pm 12 \text{ K}$ . The temperature decreases from an average value of  $85 \text{ K}$  at the start of the run to  $55 \text{ K}$  at the end of the run. The mean temperature throughout the four runs at the middle of the run is  $65 \text{ K}$ , which compares well with the calculated temperature of  $68 \text{ K}$  in Table 2.

The measured drop in temperature can be compared with the measured drop in the velocity, assuming that the Mach number is constant throughout the run. This assumption is a good one, given that the angle of the oblique shock waves visualized in the high-speed schlieren measurements did not vary throughout the run. Using the fact that velocity and temperature are related to each other through the relation

$$u = M\sqrt{\gamma RT} \quad (34)$$



The measured velocity drop of 140 m/s over the run time produces a temperature drop of approximately 20 m/s. The measured temperature drop is between 25 and 30 m/s with an uncertainty of  $\pm 12$  m/s, which is consistent with the velocity-based calculated temperature decrease.

It should be noted that these measurements are the lowest-temperature absorption measurements of oxygen temperature that can be found in the literature. The fact that the comparisons are consistent with the computations show that this method is a viable method for measurement of very low gas temperatures.

Total temperature and pitot measurements are being performed at these conditions in the Ludwig tube facility, which will provide a better idea of the nozzle Mach number and the nozzle reservoir conditions. Once this data is available we will produce axisymmetric time-resolved temperature and velocity computations produced using the commercial code Fluent that will allow direct comparison of the time-resolved measured and computed distributions of temperature and velocity.

## 8 Conclusions and Future Work

We have designed a new sensor for the Mach number and angle of attack in a supersonic combustion ramjet engine, using VCSEL-based absorption measurements. The method uses retroreflection to very accurately determine the freestream velocity and the change in absorbance with linestrength over the 8 transitions available to the laser to determine the effect of angle of attack, determining the conditions using nonlinear least-squares fitting of the absorption spectrum against a database of computed spectra. The absorbance has been computed assuming two-dimensional analytical shock theory. Simulation of absorption spectra with noise has been performed and has shown that the Mach number can be calculated very precisely for a given angle of attack, to less than  $\pm 0.02$  from the correct value. The precision of the angle of attack measurement is lower, with an uncertainty at Mach 8 and  $\alpha = 0.2$  of  $\pm 0.25$  degrees, for signals with no added random noise. The fits for angle of attack appear to be susceptible to convergence to a local, rather than a global, minimum using our fitting routine. This dependence can be minimized by selecting several start points for the least-squares fits and choosing the final fit with the lowest residual. High-frequency Gaussian noise, up to 50 % of the peak signal height, did not have a strong effect on the fitted velocity, but can have a significant effect on the temperature measurements. This sensitivity means that temperature measurements require a signal-to-noise ratio of 10 or greater to give a sensible value for angle of attack, because the peaks in the shock layers have approximately 10 % of the signal in the freestream. Our inability to fit for shock layer properties in the inlet tests in Sec. 7 is consistent with the findings of the theoretical treatment.

In addition to formulating the theoretical basis for the measurements, we have calculated the expected heat flux to the inlet plates for this simple configuration, to predict the peak temperature attained by the plates during a flight test of the type experienced in the HyShot flight program. The results of this calculation indicate that the peak temperature will not increase by more than 60 K over the time required for a flight to decrease its altitude from 65 000 m to 23 000 m at a flight Mach number of 8. Tests of the laser system have been performed over this range of temperatures, and show that the optical system is still able to operate effectively, though there may be a DC offset added to the signal. This offset can easily be accounted for without causing a systematic error. Experiments have also been performed in a combustion-heated facility with freestream gas at temperatures of up to 600° C, the maximum expected temperature in the shock layer for a Mach 10 flight test. The measurements performed in this facility were able to operate for 10 minutes at this high temperature without any adverse effect on the measurement despite the hot gas passing the optical system via an open cavity, provided the optical and electronic components were flushed with room-temperature nitrogen. This indicates that the electrical and optical components in the system should be robust enough to survive and keep taking measurements at the peak expected inlet temperature during a flight test.

Measurements of flow velocity and temperature have been performed in a hypersonic Ludwig

tube facility, and these measurements were consistent with calculations performed using a one-dimensional nozzle code, after the nozzle's displacement thickness had been accounted for. The experiments were able to measure velocity to within  $\pm 40$  m/s and temperature to within  $\pm 15$  K. The experiments showed that instrumenting a two-plate inlet was capable of adequately measuring velocity and temperature at these conditions, and that increasing the path length did not necessarily help to increase the signal-to-noise ratio of the measurements in this case. Four passes through an inlet with a tip separation of 200 mm provided enough signal to measure at the low temperatures tested in these experiments.

Future work will be directed at reducing the susceptibility of the system to vibration, as this appears to be the largest source of uncertainty in the measurements. Vibration tests are being conducted to determine the cause of the susceptibility to vibration and reduce it by making the system move as a whole rather than having the two parts of the system move independently. Once the optical system has been made more stable, we will conduct more experiments in the USQ facility to determine the feasibility of the angle of attack measurement.

We attempted in this project, unsuccessfully, to increase the bandwidth of the log-ratio detector above the 45 kHz of the log102 detector circuit used for these experiments. Although we implemented a detection circuit based upon the higher-bandwidth log114 log-ratio amplifier, the peak noise of this circuit occurred at the frequencies at which we were trying to perform our measurements. This noise could therefore not be filtered out of the system, and so we went back to using the log102. In the final year of the project we intend to investigate wavelength modulation detection for these measurements, to increase the scan rate to 1 kHz or higher. Scanning at these higher rates has the advantage of turning the effect of mechanical vibration on absorbance into a DC offset on the spectrum rather than a sinusoidal interference, making the offset much easier to remove.

## Acknowledgement

This work was funded by the US Air Force Asian Office of Aerospace Research and Development (AOARD) grant 084019 and the authors gratefully acknowledge this. We also thank Associate Professor David Buttsworth for running the tests in the University of Southern Queensland's Ludwig tube facility.

## References

- Allen, M. G., Carleton, K. L., Davis, S. J., Kessler, W. J., Otis, C. E., Palombo, D. A. and Sonnenfroh, D. M. (1995), 'Ultrasensitive dual-beam absorption and gain spectroscopy: Applications for near-infrared and visible diode laser sensors', *Applied Optics* **34**(18), 3240–3249. [3.3](#)
- Anderson, J. D. (1989), *Hypersonic and High Temperature Gas Dynamics*, 1<sup>st</sup> edn, McGraw-Hill. [5.3](#)
- Anderson, J. D. (1990), *Modern Compressible flow with Historical Perspective*, 2<sup>nd</sup> edn, McGraw-Hill. [3.1](#), [3.1](#), [5.2](#)
- Anderson, J. D. (1995), *Computational Fluid Dynamics - The Basics with Applications*, 1st edn, McGraw-Hill. [5.5](#), [5.5](#)
- Brown, L. R. and Plymate, C. (2000), 'Experimental line parameters of the oxygen A-band at 760 nm', *Journal of Molecular Spectroscopy* **199**(2), 166–179. [4](#)
- Buttsworth, D. R. and Smart, M. K. (2010), Development of a ludwig tube with free piston compression heating for scramjet inlet starting experiments, in '48<sup>th</sup> Aerospace Sciences Meeting Including the New Horizons Forum and Aerospace Exposition', Orlando, FL. [7](#)

- Eckert, E. R. G. (1955), ‘Engineering relations for friction and heat transfer to surfaces in high velocity flow’, *Journal of the Aeronautical Sciences* **22**(8), 585–587. [5](#), [5.3](#)
- Griffiths, A. D. and Houwing, A. (2005), ‘Diode laser absorption spectroscopy of water vapor in a scramjet combustor’, *Applied Optics* **44**(31), 6653–6659. [1.2](#)
- Heiser, W. H. and Pratt, D. T. (1994), *Hypersonic Airbreathing Propulsion*, AIAA Education Series, 1<sup>st</sup> edn, AIAA. [1](#)
- Ho, S.-Y. and Paull, A. (2006), ‘Coupled thermal, structural and vibrational analysis of a hypersonic engine for flight test’, *Aerospace Science and Technology* **10**(5), 420–426. [5](#)
- Hohmann, A. (2008), *Determination of the Linestrength for Oxygen and Methane at Room and Higher Temperatures using Tuneable Diode Laser Absorption Spectroscopy*, Diploma thesis, Universitaet Stuttgart. [4](#)
- Humlíček, J. (1982), ‘Optimised computation of the Voigt and complex probability functions’, *Journal of Quantitative Spectroscopy and Radiative Transfer* **27**(4), 437–444. [3.2](#)
- Jacobs, P. A. (1998), MBCNS: A computer program for the simulation of transient, compressible flows; 1998 update, Technical report, Department of Mechanical Engineering, University of Queensland. [3](#)
- Lackner, M., Totschnig, G., Winter, F., Ortsiefer, M., Amann, M.-C., Shau, R. and Roskopf, J. (2003), ‘Demonstration of methane spectroscopy using a vertical-cavity surface-emitting laser at 1.68  $\mu\text{m}$  with up to 5 MHz repetition rate.’, *Measurement Science and Technology* **14**, 101–106. [1.1](#)
- Liu, X., Jeffries, J. B. and Hanson, R. K. (2007), ‘Measurement of non-uniform temperature distributions using line-of-sight absorption spectroscopy’, *AIAA Journal* **45**(2), 411–419. [3](#)
- Long, J. (2008), *Flight Hardening Procedures for the Application of Laser Spectroscopy to Scramjet Flight*, BE thesis, School of Aerospace, Civil and Mechanical Engineering, UNSW@ADFA. [6.1](#)
- Ma, L., Sanders, S. T., Jeffries, J. B. and Hanson, R. K. (2003), ‘Pulse detonation engine characterization and control using tunable diode-laser sensors’, *Journal of Propulsion and Power* **19**(4), 568–572. [1.2](#)
- Meador, W. and Smart, M. (2005), ‘Reference enthalpy method developed from solutions of the boundary-layer equations’, *AIAA Journal* **43**, 135–139. [5.3](#)
- Measures, R. M. (1988), *Laser Remote Chemical Analysis*, Wiley. [3.2](#), [3.2](#)
- O’Byrne, S., Altenhöfer, P. and Hohmann, A. (2007), Time-resolved temperature measurements in a shock tube facility, in ‘Proceedings of the 16<sup>th</sup> Australasian Fluid Mechanics Conference’. [1.2](#)
- O’Byrne, S., Huynh, L., Wittig, S. M. and Smith, N. S. A. (2009), Non-intrusive water vapour absorption measurements in a simulated helicopter exhaust, in ‘Proceedings of the Australian Combustion Symposium’, The University of Queensland, Brisbane, Australia. [6](#)
- Odam, J., Neely, A. J., Stewart, B. and Boyce, R. R. (2005), Heating analysis of a generic scramjet, in ‘AIAA Paper 2005-3338’, AIAA/CIRA 13<sup>th</sup> International Space Planes and Hypersonics Systems and Technologies Conference, Capua, Italy. [5](#), [5.4](#), [5.8](#), [5.9](#)



- Pavone, F. S. and Inguscio, M. (1992), ‘Frequency- and wavelength-modulation spectroscopies: Comparison of experimental methods using an AlGaAs diode laser’, *Applied Physics B* **56**, 118–122. [3.3](#)
- Quine, B. M. and Drummond, J. R. (2002), ‘GENSPECT: a line-by-line code with selectable interpolation error tolerance’, *Journal of Quantitative Spectroscopy and Radiative Transfer* . [4.1](#)
- Ritter, K. J. and Wilkerson, T. D. . (1987), ‘High-resolution spectroscopy of the oxygen *A* band’, *Journal of Molecular Spectroscopy* **121**(1), 1–19. [4](#)
- Robichaud, D. J., Hodges, J. T., Brown, L. R., Lisak, D., Maskowski, P., Yeunga, L. Y., Okumuraa, M. and Miller, C. E. (2008), ‘Experimental intensity and lineshape parameters of the oxygen *A*-band using frequency-stabilized cavity ring-down spectroscopy’, *Journal of Molecular Spectroscopy* **248**(1), 1–13. [4](#)
- Rothman, L. S., Jacquemart, D., Barbe, A., Benner, D. C., Birk, M., Brown, L., Carleer, M. and *et al.*, C. C. (2005), ‘The HITRAN 2004 molecular spectroscopic database’, *Journal of Quantitative Spectroscopy and Radiative Transfer* **96**(2), 139–204. [3.2](#)
- Sanders, S. T., Jenkins, T. P. and Hanson, R. K. (2000), Diode laser sensor system for multi-parameter measurements in pulse detonation engine flows, in ‘36<sup>th</sup> AIAA/ASME/SAE/ASEE Joint Propulsion Conference and Exhibit’, Huntsville, AL. [1.2](#)
- Sanders, S., Wang, J., Jeffries, J. B. and Hanson, R. K. (2001), ‘Diode laser absorption sensor for line-of-sight temperature distributions’, *Applied Optics* **40**(24), 4404–4415. [3](#)
- Smart, M. K., Hass, N. E. and Paull, A. (2006), ‘Flight data analysis of the HyShot 2 scramjet flight experiment’, *AIAA Journal* **44**(10), 2366–2375. [5](#)
- Soda, H., Igra, K., Kitahara, C. and Suematsu, Y. (1979), ‘GaInAsP/InP surface-emitting injection lasers’, *Japan Journal of Applied Physics* **18**(12), 2329–2330. [1.1](#)
- Srinivasan, S., Tannehill, J. C. and Weilmuenster, K. J. (1987), Simplified curve fits for the thermodynamic properties of equilibrium air, NASA Reference Publication 1181, NASA. [5.2](#), [5.4](#)
- Upschulte, B. L., Miller, M. F. and Allen, M. G. (2000), ‘Diode laser sensor for gasdynamic measurements in a model scramjet combustor’, *AIAA Journal* **38**(7), 1246–1252. [1.2](#)
- van Driest, E. R. (1956), ‘The problem of aerodynamic heating’, *Aeronautical Engineering Review* **15**(10), 26–41. [5.4](#)
- Villareal, R. and Varghese, P. (2005), ‘Frequency-resolved absorption tomography with tunable diode lasers’, *Applied Optics* **44**(31), 6786–6795. [3](#)
- Webster, L., O’Byrne, S. and Houwing, A. F. P. (2005), Determination of temperature distributions in air using a scanning vertical-cavity surface-emitting laser, in ‘Proceedings of the 4<sup>th</sup> Australian Conference on Laser Diagnostics in Fluids Mechanics and Combustion’. [3](#), [3.2](#)
- Williams, S., Barone, D., Barhorst, T., Jackson, K. and Lin, K.-C. (2006), Diode laser diagnostics of high speed flows, in ‘AIAA International Space Planes and Hypersonic Systems and Technologies Conference, AIAA 2006-7999’, Canberra, Australia. [1.2](#)
- Zhang, F.-Y., Fujiwara, T. and Komurasaki, K. (2001), ‘Diode-laser tomography for arcjet plume reconstruction’, *Applied Optics* **40**(6), 957–964. [3](#)

Zhou, X., Jeffries, J. B., Hanson, R. K., Li, G. and Gutmark, E. J. (2007), ‘Wavelength-scanned tunable diode laser temperature measurements in a model gas turbine combustor’, *AIAA Journal* **45**(2), 420–425. [1.2](#)

## Appendix

### A. Personnel Supported

The main investigators on this project were Dr. S. O’Byrne, Ph.D. candidate S. M. Wittig, Dip. Ing. student A. Hohmann and undergraduate thesis students J. Long and L. Huynh. Other investigators who provided input into the results were Dr. T. McIntyre, Dr. A. J. Neely and Prof. R. R. Boyce.

The University of Southern Queensland’s Ludwig tube facility, operated by Assoc. Prof. David Buttsworth, was supported by this grant, providing the hypersonic conditions in which the sensor could be tested.

### B. Publications

- S. O’Byrne, S. M. Wittig, “Measurement of hypersonic inlet flow using diode laser absorption spectroscopy,” Proceedings of the 8th Australian Space Sciences Conference, September 29–October 1, 2008, Canberra, Australia.
- J.P. Long, S. O’Byrne and A.J. Neely, “Two-dimensional heat transfer analysis of a generic scramjet inlet,” Proceedings of the 8th Australian Space Sciences Conference, September 29–October 1, 2008, Canberra, Australia.
- A. Hohmann, S. O’Byrne, “Oxygen linestrength measurements in a high-temperature gas cell,” Proceedings of the 5<sup>th</sup> Australian Conference on Laser Diagnostics in Fluid Mechanics and Combustion, December 1–3, 2008, Perth, Australia.
- L. Huynh and S. O’Byrne, “Water Vapour Absorption Spectroscopy in a Simulated Helicopter Exhaust using Vertical-Cavity Surface-Emitting Lasers” AIAA Student Conference, Melbourne, Australia, October 2009.
- S. O’Byrne, L. Huynh, S. M. Wittig and N. S. A. Smith, “Non-intrusive Water Vapour Absorption Measurements in a Simulated Helicopter Exhaust”, Proceedings of the Australian Combustion Symposium, Brisbane, Australia, December 2–4, 2009.
- L. Huynh and S. O’Byrne, “Water Vapour Absorption Spectroscopy in a Simulated Helicopter Exhaust using Vertical-Cavity Surface-Emitting Lasers” AIAA paper 2010-1599, 48th AIAA Aerospace Sciences Meeting Including the New Horizons Forum and Aerospace Exposition, Orlando, Florida, Jan. 4–7, 2010 (Same content as above paper, re-presented by invitation).

### C. Interactions

This work was presented at the following meetings:

- The 8<sup>th</sup> Australian Space Science Conference, Canberra, December 2008.
- The 48<sup>th</sup> AIAA Aerospace Sciences Meeting, Orlando, Florida, January 2010.
- The 5<sup>th</sup> Australian Combustion Symposium, Brisbane, December 2009.
- The AIAA Student Conference, October 2009.
- The 5<sup>th</sup> Australian Conference on Laser Diagnostics in Fluid Mechanics and Combustion, Perth, December 2008.

This work will be used to design a flight-test TDLAS sensor for an axially symmetric inlet, as part of the SCRAMSPACE tests that will be conducted by a consortium led by the University of Queensland in 2012.

## **D. Inventions**

None at the moment.

## **E. Honors/Awards**

- This AOARD support has in part led to a successful application to the Australian Space Research Program for AUD 5 Million in funding for a flight test, including AUD 794 000 for development of the diode laser absorption sensor, concentrating on testing a sensor like the one produced here on a hypersonic flight test in 2012.
- The paper ‘Water Vapour Absorption Spectroscopy in a Simulated Helicopter Exhaust using Vertical-Cavity Surface-Emitting Lasers’ by L. Huynh and S. O’Byrne won the best paper award at the Australasian Branch of the AIAA Student conference.
- PhD Student S. Wittig won a 2000 UK pound competitive stipend from the Royal Aeronautical Society to perform tests at subsonic and transonic speeds in the DSTO transonic facility using O<sub>2</sub> diode laser absorption spectroscopy with ideas based upon this work
- The presentation ‘Taming the beast: the role of non-intrusive laser diagnostics in vehicle emissions measurement’ by S. Wittig won a \$1 000 prize for best presentation at the UNSW energy showcase in Sydney, Australia.